ACCSCIENCE PUBLISHING

International Journal of Bioprinting

REVIEW ARTICLE

Extrusion-based three-dimensional bioprinting of osteochondral scaffolds: Strategies using hydrogel/thermoplastic combinations

Mingzu Du[1]*, Giuseppe Tronci[1,2], Xuebin B. Yang[1], and David J. Wood[1,3]*

[1]Biomaterials and Tissue Engineering Research Group, School of Dentistry, University of Leeds, Leeds, West Yorkshire, United Kingdom

[2]Clothworkers' Centre for Textile Materials Innovation for Healthcare, School of Design, University of Leeds, Leeds, West Yorkshire, United Kingdom

[3]Bragg Centre for Materials Research, University of Leeds, Leeds, West Yorkshire, United Kingdom

(This article belongs to the *Special Issue: Three-Dimensional (3D) Bioprinting for Tissue Engineering and Food Printing*)

Abstract

Osteochondral defects remain a major clinical challenge due to the complex hierarchical structure, marked mechanical gradients, and distinct biological requirements of cartilage, calcified cartilage, and subchondral bone. Extrusion-based three-dimensional bioprinting has emerged as a promising strategy for osteochondral repair, enabling the spatially controlled deposition of cells, biomaterials, and bioactive factors to fabricate constructs with region-specific compositions and architectures. Among the available material systems, combinations of hydrogels and thermoplastics have attracted increasing attention, as they integrate the favourable biological microenvironment of hydrogels with the mechanical strength, structural stability, and printability of thermoplastics. This synergy makes them particularly suitable for the fabrication of biomimetic osteochondral scaffolds with multiphasic and gradient features. This review systematically summarises the application of hydrogel/thermoplastic combinations in extrusion-based bioprinting for osteochondral repair, with particular emphasis on their role in addressing the structural, mechanical, and biological requirements of osteochondral regeneration. It discusses the design requirements for osteochondral scaffolds, the properties and crosslinking strategies of hydrogel bioinks, the function of thermoplastic frameworks in mechanical reinforcement, and current approaches for constructing multilayered and gradient scaffolds. The review also analyses current limitations, including challenges related to printability, material compatibility, interlayer bonding, degradation mismatch, and long-term functional performance. Overall, this work provides a comprehensive overview of hydrogel/thermoplastic composite systems and highlights their potential to advance the development of clinically relevant bioprinted scaffolds for osteochondral repair.

Keywords: Extrusion bioprinting; Parameter optimisation; Hydrogel bioinks; Thermoplastic printing; Osteochondral repair

***Corresponding authors:**
Mingzu Du
(dnmdu@leeds.ac.uk)
David J. Wood
(D.J.Wood@leeds.ac.uk)

Citation: Du M, Tronci G, Yang XB, Wood DJ. Extrusion-based three-dimensional bioprinting of osteochondral scaffolds: Strategies using hydrogel/thermoplastic combinations. *Int J Bioprint*. 2026;12(3):026140122. doi: 10.36922/IJB026140122

Received: March 30, 2026

Revised: May 1, 2026

Accepted: May 7, 2026

Published online: May 11, 2026

1. Introduction

The osteochondral unit possesses a unique and highly complex hierarchical structure, and defects in this region remain difficult to repair because of its avascular and aneural nature.[1] Early-stage osteochondral abnormalities are often clinically silent and may not present with obvious symptoms. Arthroscopic osteochondral lesions are commonly classified according to lesion size and cartilage depth, with most lesions falling within grade 2 (less than 50% of cartilage depth) or grade 3 (more than 50%), both of which may progress to osteoarthritis if left untreated.[2] Once the defect extends into the subchondral bone, implantation of multiphasic scaffolds that better recapitulate the native osteochondral architecture may become necessary.[3] Such scaffolds must meet stringent requirements for mechanical performance, biodegradability, biocompatibility, and regenerative capacity.

Three-dimensional (3D) bioprinting offers a promising strategy for osteochondral repair because it enables the controlled spatial organisation of cells, biomaterials, and bioactive molecules within architecturally defined constructs.[4] In principle, multilayered or multiphasic structures can be fabricated to more closely mimic the anatomical and functional heterogeneity of native tissues.[5] For example, in articular cartilage, collagen fibres are aligned parallel to the joint surface in the superficial zone and gradually reorient towards a perpendicular direction near the calcified cartilage layer.[6] This zonal organisation highlights the importance of controlling not only scaffold composition, but also the spatial arrangement of structural and biological cues within the printed construct. In collagen-based systems, fibril organisation may also be influenced by co-formulated matrix components such as hyaluronic acid, which can constrain fibril growth through molecular crowding and adhesive interactions.[7]

A range of bioprinting techniques has been explored for osteochondral regeneration. Inkjet bioprinting can be used to deposit different cell types, including mesenchymal stem cells (MSCs) and articular chondrocytes.[8] Laser-assisted bioprinting enables high-resolution cell patterning without nozzle clogging, although its complexity and cost have limited its broader application in this field.[9] Stereolithography uses patterned light to crosslink photopolymerisable resins and can generate highly precise structures, but the range of suitable biocompatible materials remains limited.[8] Among these approaches, extrusion bioprinting has become the most widely used technique for osteochondral scaffold fabrication.[10] It is compatible with a broad range of hydrogel-based bioinks with different rheological properties, and supports the fabrication of large-scale 3D constructs with high cell density,[11] and can also be adapted for printing thermoplastic materials under controlled temperature conditions.[12] Nevertheless, the relatively limited printing resolution remains an important constraint.[13]

In extrusion bioprinting, printability is determined by the interplay between material properties, process parameters, and construct design. Printing resolution reflects the spatial distribution of deposited material within the x–y plane, while dimensional fidelity in the z-axis contributes to structural integrity.[14] The minimum feature size that can be achieved depends on the rheological behaviour of the bioink, the printing conditions, and the scaffold geometry.[15] At the same time, nozzle diameter strongly influences the shear stress experienced by encapsulated cells, with smaller nozzles increasing the risk of cell damage. Additional parameters, such as printing speed and extrusion pressure, must also be carefully optimised, particularly when complex osteochondral architectures are required.

These considerations make osteochondral scaffold fabrication especially challenging, as the selected materials must satisfy biological, mechanical, and processing requirements simultaneously. Current strategies are therefore increasingly focused on multiphasic constructs that combine a cartilage-mimicking phase, typically based on soft hydrogels, with a bone-mimicking phase composed of stiffer materials such as thermoplastics. In some cases, additional interfacial layers are introduced to improve the structural and biological integration between phases. For example, Wu *et al.*[16] developed a trilayer biomimetic scaffold composed of polycaprolactone (PCL), chondrocyte-laden gelatine methacrylate (GelMA), and a compact PCL/nano-hydroxyapatite/tasquinimod interlayer that mimicked calcified cartilage and helped preserve the biological independence of the cartilage-like phase. Similarly, Liu *et al.*[17] reported a PCL/bone marrow MSC (BMSC)-laden methacrylated hyaluronic acid scaffold with an additional diclofenac sodium-containing methacrylated hyaluronic acid layer to address joint inflammation, resulting in improved joint function. These examples illustrate that hydrogel/thermoplastic combinations can replicate not only the spatial organisation and mechanical gradient of the native osteochondral unit but also support region-specific biological functions.

This review provides an overview of recent strategies for osteochondral repair using extrusion-based multiphasic 3D bioprinting. It first summarises the structural complexity of the osteochondral unit and the challenges associated with endogenous repair. It then discusses the working principles and advantages of extrusion bioprinting for the fabrication of multiphasic scaffolds. Finally, it examines

material selection for cartilage- and bone-mimicking phases, along with the key considerations for matching these materials to the printing platform and for designing rational osteochondral constructs (Figure 1).

2. The osteochondral unit

2.1. Physiological basis for osteochondral scaffold design

The osteochondral unit is a complex hierarchical tissue composed of articular cartilage, calcified cartilage, and subchondral bone, with marked variations in cellular composition, matrix organisation, vascularity, and mechanical properties across its depth.[18] Articular cartilage mainly consists of chondrocytes embedded in extracellular matrix (ECM) and is divided into superficial, transitional, and deep zones, each characterised by distinct cell morphology and collagen organisation that support resistance to shear and compressive forces.[19] Calcified cartilage forms a critical transitional interface between articular cartilage and subchondral bone, helping to reduce stiffness mismatch and facilitate load transfer across the osteochondral unit.[19,20] Beneath this layer, subchondral bone can be divided into the subchondral bone plate and subchondral trabecular bone, which together provide structural support and a porous microenvironment containing bone marrow and MSCs with osteochondral differentiation potential.[21,22]

Bone tissue is dynamically remodelled through the coordinated activities of osteoblasts, osteocytes, and osteoclasts, which are essential for maintaining skeletal homeostasis. In the osteochondral unit, differences in the structure and porosity of the subchondral bone plate and trabecular bone influence vascular and neural distribution, thereby supporting nutrient transport and

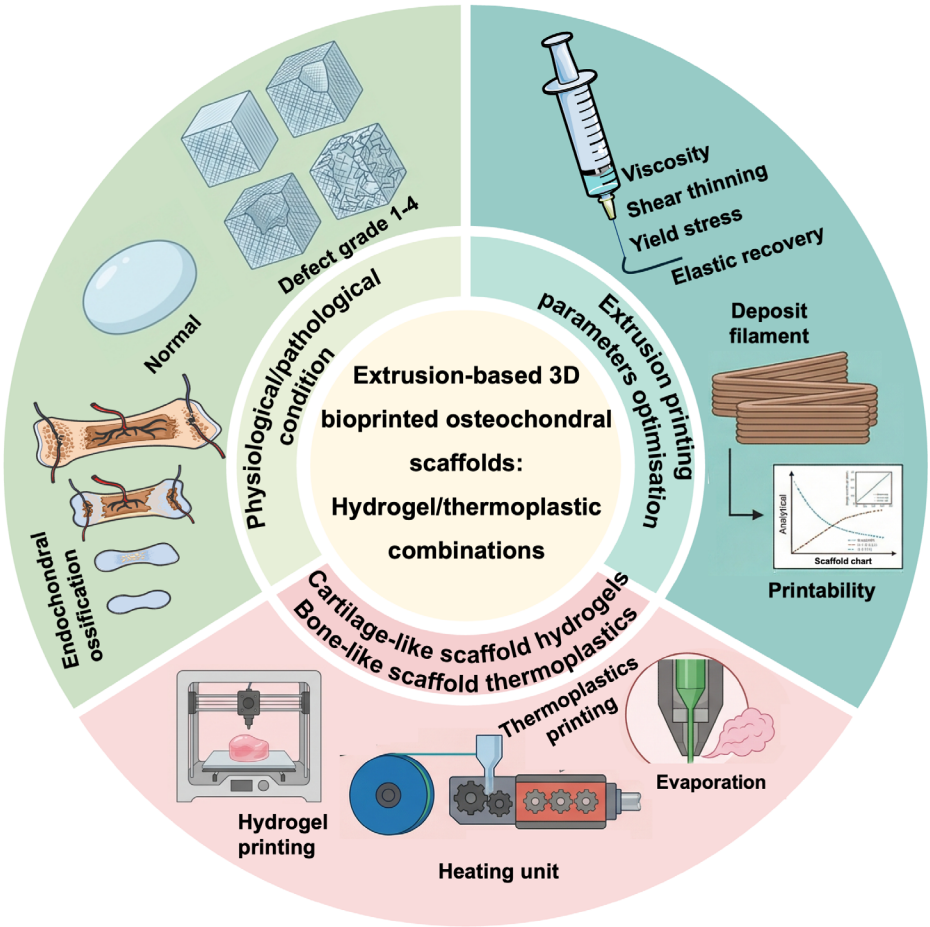

Figure 1. Overview of extrusion-based three-dimensional (3D) bioprinting of osteochondral scaffolds using hydrogel/thermoplastic combinations. The schematic illustrates the physiological and biological characteristics of the osteochondral unit, the key rheological and printing-related parameters that affect bioink printability, and the fabrication concept for composite scaffolds integrating cartilage-like hydrogel regions with bone-like thermoplastic support structures. Created by the authors using Microsoft PowerPoint and Adobe Illustrator.

metabolic activity within the bone compartment.[23,24] In addition, the osteochondral unit exhibits a pronounced mechanical gradient. The compressive modulus increases progressively from articular cartilage to subchondral bone. In articular cartilage, the modulus ranges from 0.2 to 6.44 MPa from the superficial to the deep zone. In contrast, the subchondral bone plate and trabecular bone display much higher moduli, at 18–22 GPa and 0.1–0.9 GPa, respectively.[23] These biological and mechanical heterogeneities are important for normal tissue function but also pose major challenges for the design of biomimetic scaffolds for osteochondral repair.

2.2. Pathological conditions of osteochondral tissue

When diagnosing osteochondral abnormalities, the entire osteochondral unit should be evaluated rather than the articular cartilage alone, because lesions often begin at the cartilage surface and progressively extend into deeper tissues.[24] According to the International Cartilage Repair Society classification (Figure 1), osteochondral defects are divided into five grades, ranging from grade 0 for normal cartilage to grade 4, in which damage penetrates the subchondral bone.[2] Hence, repair strategies must address the structural and functional complexity of the entire osteochondral unit.

2.3. Current repair strategies for osteochondral defects

Mature articular cartilage is avascular and aneural, with very limited intrinsic healing capacity, making repair of osteochondral defects highly challenging.[1] Osteochondral lesions are frequently identified in the knee, with grade 2 and 3 defects being particularly common.[18] Current repair strategies can be broadly divided into scaffold-free and scaffold-based approaches. For lesions confined to the cartilage layer, scaffold-free strategies based on cell aggregates may be used, offering advantages such as reduced immunogenicity and relatively simple preparation.[21] Cell sources for these approaches include tissue-specific cells, such as chondrocytes, as well as progenitor cells, including MSCs.[25,26] However, scaffold-free constructs often show insufficient mechanical strength and limited anchorage to the underlying subchondral bone, which restricts their application in load-bearing osteochondral repair.[27] For defects involving both cartilage and subchondral bone, particularly grade 4 lesions, scaffold-based strategies are more commonly employed. In these systems, the scaffold provides a 3D microenvironment for cell adhesion, proliferation, and differentiation while also contributing to mechanical support.[28] Accordingly, effective osteochondral scaffolds should possess appropriate mechanical properties, support the regulation of cell behaviour, and exhibit a degradation profile compatible with the rate of tissue regeneration.[21]

3. Extrusion three-dimensional bioprinting

Several 3D bioprinting techniques have been explored for osteochondral repair. Extrusion bioprinting accommodates more viscous bioinks, supports higher cell densities, and provides greater structural integrity, although its resolution is typically lower, at around 100 μm.[29,30] Depending on the driving mechanism, extrusion bioprinting can be further divided into pneumatic-, piston-, and screw-driven systems.[31] It may also be categorised according to the printing environment: direct ink writing, printing in a coagulation bath, printing in a support bath, and co-axial extrusion.[32]

Direct ink writing is one of the most common extrusion-based approaches and relies heavily on the shear-thinning behaviour of the bioink, thereby placing stringent demands on rheological optimisation.[32] For example, Wu *et al.*[33] used two deccellularised natural cartilage-based bioinks to fabricate a gradient bilayer scaffold for the repair of an osteochondral defect. The study included extensive optimisation of pre-crosslinking, nano-hydroxyapatite incorporation, and layer composition.[33] Printing in a coagulation bath reduces reliance on intrinsic bioink rheology by inducing rapid gelation in a liquid medium, though it may be associated with liquid backflow and nozzle blockage.[34] Co-axial extrusion enables the simultaneous deposition of concentric material streams and is particularly promising for recreating the stiffness gradient of the bone–cartilage interface or fabricating hollow fibres for improved nutrient transport.[35] By contrast, support-bath printing uses granular or colloidal materials to temporarily stabilise deposited structures, facilitating the fabrication of complex architectures, although post-printing removal of the support medium may compromise dimensional fidelity.[36]

3.1. Rheological properties of bioinks

The rheological requirements of bioinks vary with the printing mechanism and must therefore be tailored to the specific bioprinting platform. For example, pneumatic extrusion generally requires viscosities of approximately 30 mPa·s to 6×10^7 mPa·s, whereas mechanically driven systems usually require viscosities exceeding 6×10^7 mPa·s.[37] Material type is also important. Thermoplastic polymers such as PCL and poly(3-hydroxybutyrate) are typically extruded as molten filaments,[38] whereas hydrogel-based extrusion bioprinting usually requires post-printing or *in situ* crosslinking, and excessive shear stress must be avoided to preserve cell viability.[39]

Regardless of the material system, rheological optimisation remains essential, particularly with respect to viscosity, shear-thinning behaviour, viscoelasticity, and yield stress. Bioinks are typically non-Newtonian and most commonly exhibit shear-thinning behaviour, which facilitates extrusion and helps maintain shape fidelity after deposition. Although higher viscosity generally improves print fidelity,[40] it may also increase shear stress and reduce the viability of encapsulated cells. Viscoelasticity, commonly characterised by the storage modulus (G′) and loss modulus (G″),[41] is also critical for filament stability and structural integrity after printing. Yield stress is also important. Increasing yield stress can improve construct stiffness and shape retention, but excessively high values may impair flow through the nozzle.[42] The sol–gel transition behaviour of bioinks can also be evaluated from changes in G′ and G″ under stresses below and above the yield point (Figure 2A).[43]

Biological and therapeutic components, including cells, growth factors, cytokines, and drugs, can further alter bioink rheology. Encapsulated cells may interfere with interactions between crosslinkable groups and prolong gelation time.[44] At higher cell densities, they may also contribute to the composite behaviour of the bioink, in some cases enhancing its mechanical properties and viscoelasticity.[45]

3.2. Scaffold printability and parameter optimisation

Printability is a key parameter in bioink development and evaluation. In extrusion-based bioprinting, it mainly comprises extrudability, filament formation, and shape fidelity.[46] Because rheology strongly influences extrusion behaviour and structural fidelity, it is usually optimised first.[47] Among rheological parameters, the flow consistency index (K) and flow behaviour index (n) are particularly important.[46,48] K reflects flow resistance, whereas n indicates the degree of shear-thinning behaviour. For hydrogel-based bioinks such as alginate and GelMA, K typically falls within 0.01–10 Pa·s^n.[49] In general, bioinks with low-to-moderate K and $n < 1$ are preferred because they can flow readily during extrusion and recover viscosity after deposition, thereby supporting both printability and cell viability. These non-Newtonian flow characteristics are commonly described by the Ostwald-de Waele and Herschel-Bulkley models (**Equations 1** & **2**).[50,51]

$$\eta = k\dot{\gamma}^{n-1} \quad (1)$$

$$\tau = \tau_0 + k\dot{\gamma}^n \quad (2)$$

where η is viscosity, K is the flow consistency index, $\dot{\gamma}$ is shear rate, n is the flow behaviour index, τ is shear stress, and τ_0 is the yield stress.

Extrudability is commonly assessed by the force required to overcome the yield stress.[52] Under suitable conditions, the bioink forms a continuous and homogeneous filament; otherwise, droplet-like or discontinuous extrusion may occur. Filament fusion and filament collapse tests are widely used to evaluate filament formation and shape retention. In particular, the diffusion rate (D_{fr}) quantifies lateral spreading within lattice structures, whereas the collapse area factor (C_f) reflects the ability of a filament to span gaps without gravitational deformation. Planar shape fidelity can also be assessed using the printability index (P_r, Figure 2B), with values closer to 1 indicating higher geometric accuracy.[53,54]

Following optimisation of single-layer printing,

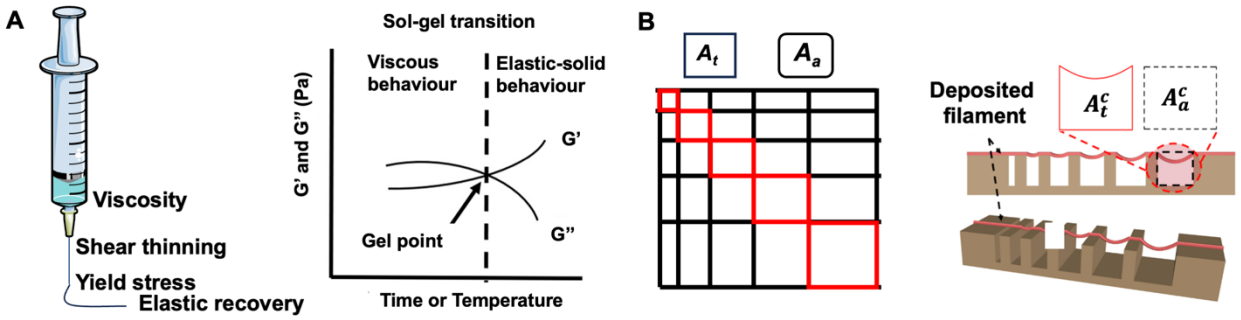

Figure 2. The rheological requirements of bioinks and the optimisation of scaffold printability. (A) Rheological properties of bioinks, viscosity and shear thinning, yield stress, and sol-gel transition. Created by the authors using Microsoft PowerPoint and Adobe Illustrator. (B) Scaffold printability and bridge evaluation models. Adapted from Habib et al.[39]
Abbreviations: A_a: Actual area; A_t: Theoretical area; G′: Storage modulus; G″: Loss modulus.

multilayer fidelity can be evaluated by comparing the printed height with the designed scaffold height. More recently, non-destructive techniques such as computed tomography (CT) and optical coherence tomography have been applied for real-time print inspection and structural analysis.[55,56] Importantly, cell-laden bioinks may behave differently from acellular inks because cells can alter rheology and extrusion behaviour. Printability is also strongly influenced by processing parameters, including printing speed, extrusion pressure, and nozzle diameter. Although these parameters are often adjusted empirically, quantitative indices such as D_{fr}, C_f, and P_r provide more objective criteria for defining an optimal printing window, and emerging machine learning approaches may further assist by predicting suitable conditions from rheological datasets.[57]

4. Scaffold design

Building on the above considerations, scaffold design in osteochondral bioprinting mainly concerns the selection and integration of region-specific materials within a multiphasic construct. To facilitate cross-study evaluation, the representative hydrogel, thermoplastic, and hybrid scaffold systems discussed in this section are compared not only by composition but also by quantitative parameters, including rheological or mechanical properties, strand or pore geometry, printing conditions, and reported biological performance. The following subsections, therefore, focus on the advantages and trade-offs of each strategy rather than presenting individual studies in isolation.

4.1. Biomimetic cartilage layer: Hydrogel

Hydrogels are widely recognised as suitable materials for mimicking the cartilage layer because they provide a hydrated and viscoelastic microenvironment that supports cell encapsulation, nutrient diffusion, and matrix deposition. During extrusion, their viscoelastic nature can also help dissipate shear stress and reduce direct cell–nozzle interactions, thereby contributing to both cell protection and structural fidelity.[58] For successful 3D bioprinting, hydrogel bioinks must exhibit an appropriate printing window, defined as the range of conditions over which satisfactory printability, structural integrity, and cytocompatibility can be maintained. In this regard, Ouyang[59] proposed distinguishing between the printing window during fabrication and that during subsequent cell culture, with the former being governed mainly by rheology, cell viability, and structural fidelity, and the latter more strongly dependent on cellular activity and long-term structural stability.

Hydrogel bioinks are typically formed through physical and/or chemical crosslinking (Figure 3), and the choice of crosslinking mechanism strongly influences their rheological behaviour, stability, and biological performance.[60] Although single-component hydrogels are widely used, they often exhibit a narrow printing window and limited functionality. As a result, increasing attention has been directed towards multi-component systems, which can broaden the printable range and improve the structural and biological properties of the resulting constructs. According to their design and preparation strategies, these bioinks can be broadly classified into multimaterial systems, interpenetrating networks, nanocomposite hydrogels, and supramolecular hydrogels.

4.1.1. Multimaterial/dual-crosslinked network bioinks

Multimaterial or dual-crosslinked bioinks are designed to combine two or more components and two crosslinking mechanisms within a single hydrogel network, so that one interaction supports extrusion or rapid filament formation, whereas the other stabilises the construct after deposition.[61] In osteochondral bioprinting, this strategy is particularly useful because it helps preserve the spatial organisation of cartilage-like, interfacial regions during handling and culture.

Oxidised alginate–gelatine is a representative example of this design principle. In this system, alginate is first oxidised to introduce aldehyde groups, which react with gelatine to form covalent bonds, while subsequent ionic crosslinking with Ca^{2+} further stabilises the printed construct.[62] This combination enables cell encapsulation and extrusion while improving post-printing integrity. Additionally, extrusion-induced alignment of crosslinked macromolecules may help guide cell orientation (Figure 4A). Recent studies from 2024 to 2026 further support this broader strategy of using dual crosslinking to reconcile biological permissiveness and printability with post-printing structural stability. For example, Lan *et al.*[63] developed a double-crosslinked cartilage bioink based on acrylated collagen, thiol-modified hyaluronic acid, and polyethylene glycol (PEG) diacrylate. The photocurable acrylated type I collagen (COLMA) + thiol-modified hyaluronic acid + polyethylene glycol formulation improved printability and shape fidelity, with post-printing filament diameters closely matching the inner diameter of the needle. For this formulation, human nasal chondrocyte viability was 85.71 ± 0.6% after bioprinting and 83.3 ± 1.2% after ultraviolet curing. After six weeks of chondrogenic culture, all three hydrogel groups supported cartilaginous extracellular matrix formation, while COLMA +thiol-modified hyaluronic acid + polyethylene glycol showed significantly higher GAG/DNA than the COLMA and COLMA + thiol-modified hyaluronic acid groups.[63] In 2025, Hashemi-Afzal *et al.*[64]

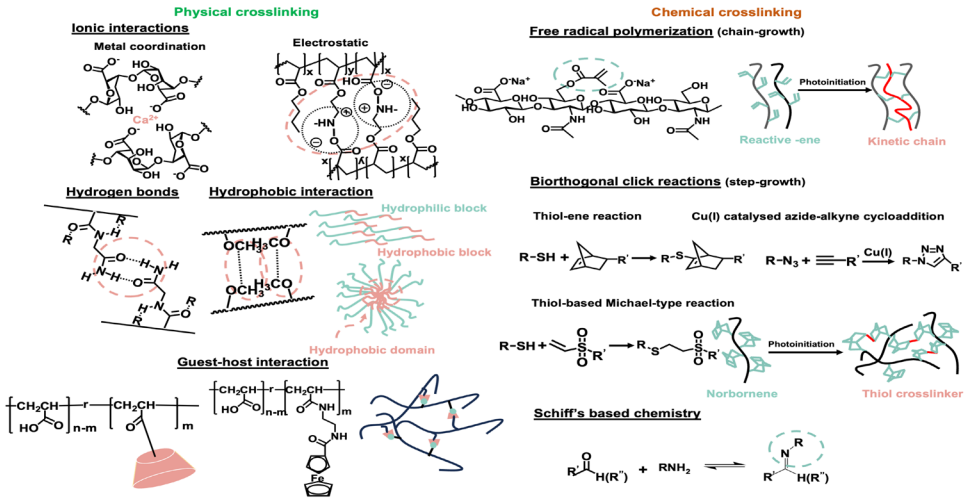

Figure 3. Crosslinking mechanisms. Physical and chemical crosslinking mechanisms used for fabricating hydrogel bioink for cartilage regeneration (selected). Created by the authors using ChemDraw and Microsoft PowerPoint.

reported a dual-crosslinked gellan gum-based system reinforced with aminolysed PCL nanofibres, achieving high structural fidelity, a compressive modulus of 232.6 kPa, about 30% mass loss over 21 days, and more than 85% cell viability after 7 days. A recent multilayer cartilage study by Çelik *et al.*[65] further showed that incorporation of PEG dimethacrylate enhanced structural integrity and reduced enzymatic degradation in zone-inspired hydrogel constructs. Mechanical testing revealed a progressive stiffness gradient, with the compressive modulus increasing from across the individual hydrogel layers, with Young's modulus increasing from approximately 31 kPa in the superficial layer to approximately 66 kPa, 106 kPa, and 128 kPa in the middle, deep, and calcified layers, respectively. *In vitro* chondrocyte studies further confirmed high cytocompatibility and zone-associated gene expression, with elevated *COL2A1* expression in the middle zone and increased *COL10A1* expression in the calcified-mimicking region.[65] Together, these studies suggest that dual crosslinking is particularly valuable when the key design challenge is not merely to print a cell-laden construct, but to preserve scaffold architecture, handling stability, and layer-specific reproducibility after printing.

However, these findings should also be interpreted with methodological caution. In many extrusion bioprinting studies, post-printing cytocompatibility is mainly evaluated by Live/Dead staining, which provides a useful but relatively static snapshot of cell membrane integrity but does not fully capture delayed cell injury, proliferation, matrix production, or spatial heterogeneity within printed filaments. Therefore, Live/Dead results should not be treated as an isolated indicator of bioink biocompatibility in extrusion-printed constructs. Instead, they should be interpreted together with extrusion-related factors that directly affect cell stress and filament-level heterogeneity. Moreover, cell viability after extrusion is not determined only by bioink composition or crosslinking chemistry, but also by nozzle geometry and printing conditions. Recent nozzle-design studies have shown that contraction angle, outlet diameter, land length, and printing speed can substantially alter shear and extensional stress during extrusion. For example, Lombardi *et al.*[66] demonstrated that custom nozzles with outlet diameters of 0.5, 0.75, and 1.0 mm and land lengths of 5 or 10 mm produced geometry-dependent cell damage, with larger contraction angles approaching 90° increasing extensional stress and reducing cell survival. Their study also noted that extrusion-related stresses may reduce cell viability to as low as 45%, depending on bioink viscosity, cell concentration, and nozzle diameter (Figure 4B). Similarly, computational fluid dynamics-guided optimisation of multi-biomaterial extrusion nozzles showed that decreasing nozzle diameter and increasing printing speed markedly increased maximum shear stress.[67] For example, at 2 mm/s, the calculated maximum shear stress decreased from about 720.79 Pa for a 0.16 mm outlet to 440.71 Pa for a 0.41 mm outlet and 394.05 Pa for a 0.51 mm outlet, whereas at 8 mm/s it increased to 1,448.58, 907.82, and 812.64 Pa, respectively. Together, these studies indicate that post-printing cytocompatibility should be reported with sufficient processing context, including nozzle geometry, extrusion speed, pressure, bioink viscosity, and, where possible, cell distribution within the filament cross-section. This is particularly important for multimaterial or dual-crosslinked systems, where rheology and gelation

kinetics may also influence cell sedimentation, local cell density, and heterogeneity during prolonged printing.[68]

However, a denser or more permanent network helps the printed construct retain its geometry, but it may also restrict cell spreading, matrix transport, and cell-mediated remodelling if the scaffold becomes too static. This concern is supported by earlier mechanistic studies in cartilage-related GelMA hydrogels.[69] At a constant polymer concentration, increasing the degree of methacrylation increased hydrogel stiffness from approximately 3.8 to 29.9 kPa and reduced swelling. This increase in stiffness was associated with more restricted chondrocyte spreading and a rounder cell morphology (Figure 4C). Similarly, studies in PEG-based hydrogels[70] showed that network structure influences not only the amount of matrix produced, but also whether that matrix remains confined to the pericellular region or expands into a broader extracellular space. Importantly, more recent evidence points in the same direction. A 2025 cartilage bioprinting study by Hosseini *et al.*[71] reported that a directional ionic crosslinking strategy generated a stiffness gradient from 39.8 ± 6.6 kPa in the softer top zone to 60.6 ± 10.9 kPa in the stiffer bottom zone. After 28 days of culture, the softer region showed higher cell density and significantly greater sulphated glycosaminoglycan deposition than the middle and bottom zones, indicating that lower local stiffness favoured cartilage-like matrix formation by chondrocytes. These findings suggest that, particularly in the cartilage-facing region, greater crosslink density should not automatically be interpreted as a biological advantage.

At the same time, the biological message is not simply that softer hydrogels are always better. What matters is whether stiffness, degradability, and stress relaxation are matched to the needs of the target tissue zone. In a methacrylated chondroitin sulphate and GelMA system designed by Ai *et al.*,[72] a formulation with an initial modulus of approximately 33 kPa was identified as favourable for MSC chondrogenesis compared with a softer formulation of about 8.4 kPa. This suggested that moderate reinforcement can still be beneficial within an appropriate biochemical context. Dynamic covalent studies reinforce this more balanced interpretation. Tavakoli and colleagues[73] showed in 2024 that dynamic dual crosslinking in hyaluronic acid hydrogels could be finely adjusted by varying the cysteine-functionalised hyaluronic acid: aldehyde-modified hyaluronic acid ratio from 100:00 to 50:50, thereby tuning the balance between disulfide and thiazolidine linkages. While thiazolidine-containing formulations formed gels immediately after mixing, the purely disulphide-crosslinked gel required about 74 min to reach the gel point. This tuning improved construct stability and biological performance, with high

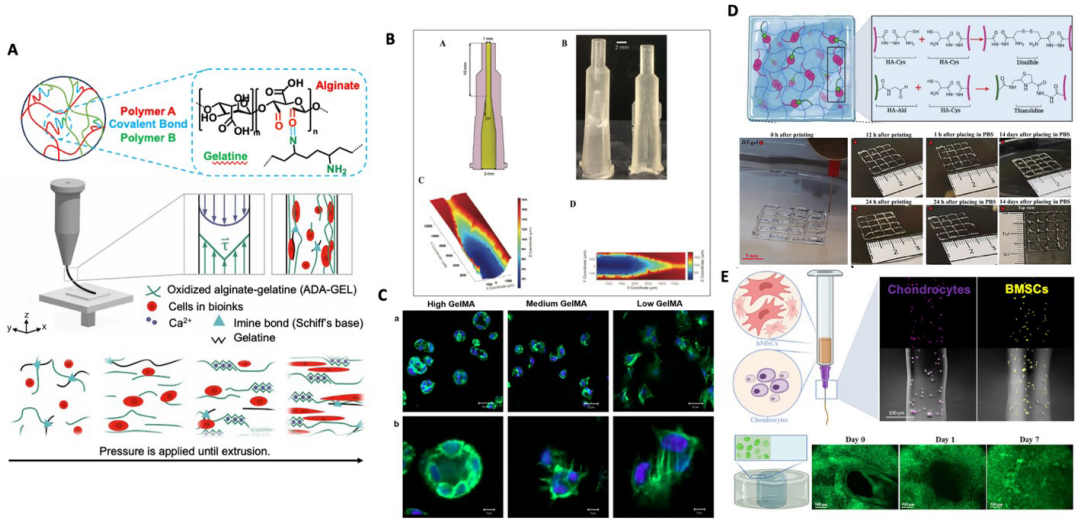

Figure 4. Multimaterial/dual-crosslinked network bioinks. (A) Multimaterial as a strategy to fabricate multi-component hydrogel bioinks, and the schematic illustration of the mechanism of bioink extrusion. Adapted from Distler et al.[75] (B) Designed nozzle analysis, including the 3D nozzle model, printed nozzle geometry, and confocal microscopy characterisation of the internal surface topology and roughness. Adapted from Lombardi et al.[66] (C) Confocal laser microscopy images of chondrocytes cultured in GelMA hydrogels for 7 days, with F-actin stained green and nuclei stained blue. Scale bar: (a) 20 μm, (b) 5 μm. Adapted from Li et al.[69] (D) Hydrogel formation and crosslinking kinetics based on disulfide and thiazolidine bond formation between HA–Cys and HA–Ald. Adapted from Tavakoli et al.[73] (E) 3D bioprinting of HA–Cys with KI hydrogels loaded with chondrocytes and hMSCs, showing printed cell-laden filaments, real-time cell movement within hollow-cylinder infill structures over 7 days, and quantified cell migration distances. Scale bar: 100 μm, 500 μm. Adapted from Tavakoli et al.[74]

Abbreviations: 3D: Three-dimensional; GelMA: Methacrylate gelatine; HA–Ald: Aldehyde-modified hyaluronic acid; HA–Cys: Cysteine-modified hyaluronic acid; hMSCs: Human mesenchymal stem cells; KI: Potassium iodide.

post-printing cell survival and more than twofold increases in the stemness markers OCT3/4 and NANOG (Figure 4D). In 2025, the same group[74] further reported ultra-fine bioprinting using a dynamic hyaluronic acid hydrogel, in which 50 mM potassium iodide provided a printing window of more than 3 h, enabled extrusion through 32-G needles with a 108 μm inner diameter, and maintained cell viability above 90% up to day 7 (Figure 4E). Collectively, these data suggest that the real design objective is not maximal stabilisation, but a balance between structural support and biological adaptability.

Taken together, multimaterial/dual-crosslinked bioinks are most suitable when the main priority is to preserve printing fidelity, spatial definition, and post-printing stability across distinct osteochondral regions. However, they may be less effective when extensive cell remodelling, rapid matrix redistribution, or a highly permissive cartilage-like microenvironment is needed. These systems should therefore be evaluated not only by printability and mechanical reinforcement, but also by whether their level of stabilisation remains compatible with the biological demands of each scaffold zone.

4.1.2. Interpenetrating network bioinks

Interpenetrating networks (IPNs) consist of two or more polymer networks that are physically interwoven. These networks remain chemically independent and are not covalently bonded to one another.[61] Compared with the multimaterial or dual-crosslinked bioinks, IPN bioinks are defined by the formation of coexisting yet independent networks that can share load while being tuned separately in terms of mechanics, transport, and biological signalling. This distinction is particularly relevant in osteochondral bioprinting, where the design challenge is not only to preserve post-printing shape, but also to achieve cartilage-like mechanical function under compression and cyclic loading.

This design logic is well illustrated by foundational cartilage-focused IPN studies. In Wang *et al.*,[76] a sulphated alginate–GelMA IPN bioink was prepared by replacing 30% of the alginate phase with alginate sulphate. The final formulation contained 1% alginate, 10% GelMA, and 0.05% photoinitiator (Figure 5A). This modification introduced sulphated glycosaminoglycan-like functionality and improved transforming growth factor (TGF)-β3 retention, reducing cumulative release by day 7 from 65.9 ± 3.8% in the non-sulphated IPN to 42.2 ± 5.8% in the sulphated IPN. Meanwhile, the compressive modulus increased to 32.48 ± 4.23 kPa, compared with 11.07 ± 1.92 kPa for GelMA alone and 6.85 ± 1.17 kPa for the sulphated alginate network alone. Although load sharing between the two networks was not measured directly, the mechanical response was clearly synergistic rather than additive. In related work, Schipani *et al.*[77] further showed that this principle could be extended through structural reinforcement, combining alginate–GelMA IPN hydrogels with 3D-printed PCL fibre networks. A double offset PCL architecture showed lower compressive stiffness than aligned PCL but still retained substantial tensile stiffness. When combined with the IPN hydrogel, this architecture led to a synergistic increase in the ramp modulus. It also generated about 24 times the hydrostatic pressure as the IPN alone under 10% compression. Together, these studies show that the value of cartilage-focused IPN systems lies not simply in increasing stiffness, but in integrating biochemical retention, printability, and mechanically cooperative reinforcement within a single platform.

More recent studies from 2024 and 2025 further clarify this distinction between double-network (DN) and ionic–covalent entanglement (ICE)-type IPN bioinks, while also revealing an important methodological issue in how bioprinted bioinks are evaluated. DN systems are generally preferred when high initial stiffness, shape retention, and resistance to deformation immediately after printing are required. For example, Wang *et al.*[78] developed an elastin-containing DN hydrogel composed of covalently crosslinked GelMA and a dynamically crosslinked hyaluronic acid-based elastin network. Under 405 nm light, the bioink gelled within 5 s and exhibited an apparent viscosity of 47,770.1 mPa·s at 0.1 s^{-1}. Mechanically, it reached about 170% strain, a toughness of approximately 45 kJ m^{-3}, and a compressive modulus of 19.85 kPa. The study also reported key printing parameters, including the use of a 23G blunt needle with an inner diameter of 0.34 mm, an extrusion pressure of 0.6–1 bar, and a print-head speed of 13–15 mm/s.[78] Biologically, this system maintained chondrocyte viability above 85% on day 1 and above 89% on day 7 (Figure 5B). It also supported earlier cell spreading and stronger collagen II staining than the other tested groups. This suggests that the increase in network toughness did not necessarily impair cartilage-like matrix formation. However, the viability data were still mainly interpreted at the construct level. Although filament morphology and construct fidelity were evaluated, the study did not directly analyse whether cells were homogeneously distributed across the filament cross-section or whether local cell damage was concentrated in regions exposed to higher extrusion-induced stress.

In a more osteochondral-specific example, Zhang *et al.*[79] identified 7% GelMA/3% methacrylated alginate as an effective DN-like formulation. It showed rapid photocrosslinking within about 5 s, could be printed at

room temperature at ≤70 kPa, and maintained 85.7% post-printing cell viability. The supplementary methods further reported a 0.3 mm needle, 0.5 mm line spacing, and an extrusion pressure increased up to 70 kPa to obtain smooth lines. The hydrogel also exhibited a swelling ratio of 916.10% ± 4.97% and degraded over more than 5 weeks. Importantly, it supported progressive upregulation of *Col2a1*, *Acan*, and *Sox9*, stronger collagen II and aggrecan deposition, and satisfactory synchronous regeneration of cartilage and subchondral bone *in vivo*. Compared with homogeneous hydrogels, neo-cartilage and neo-bone formation were further increased by 23.5% and 20.8%, respectively, suggesting that DN reinforcement can be biologically effective when matched to an osteochondral design logic rather than used purely for mechanical strengthening. Nevertheless, as with many extrusion bioprinting studies, Live/Dead staining alone cannot fully separate the effects of hydrogel composition, photocrosslinking, extrusion pressure, and nozzle-induced mechanical stress. The study successfully demonstrated spatial allocation of different cell types between osteochondral layers but did not further quantify cell distribution within individual printed filaments.

By contrast, a more reversible dual-crosslinkable IPN strategy, conceptually closer to ICE systems, was reported by Sasikumar *et al.*,[80] who combined photo-crosslinked methacrylated mucin with Ca^{2+}-crosslinked alginate and hyaluronic acid entanglement. Their HAM1075 formulation showed better filament stability than HAM1505, reached a compressive modulus of 326.70 ± 11.42 kPa, and retained about 80% of its mass after 4 weeks (Figure 5C). Biologically, hyaluronic acid-containing formulations supported better cell viability and proliferation than alginate-dominant controls, and collagen II levels increased progressively over the culture period, indicating early chondrogenic potential. Nevertheless, this evidence remains mainly short-term and *in vitro*, so it currently supports cytocompatibility and early cartilage-marker expression more strongly than mature osteochondral regeneration. In addition, because reversible or ICE-like IPN bioinks are often designed to flow, recover, and remodel during extrusion, future studies should quantify not only Live/Dead viability and proliferation, but also filament-level cell distribution, post-printing cell morphology, matrix deposition, and retention under mechanically relevant culture conditions.

Taken together, these recent studies suggest that more persistent IPN designs are advantageous for post-printing shape retention and structural support, whereas more reversible or ICE-like designs may better support resilience, cytocompatibility, and early matrix development, although *in vivo* reparative evidence remains less developed. However, current evidence remains weighted toward bulk mechanics, short-term Live/Dead viability, and early marker expression. For osteochondral applications, future IPN bioinks should therefore be evaluated using a broader set of criteria, including nozzle and pressure conditions, filament morphology, spatial cell distribution, delayed cell function, matrix deposition, and *in vivo* repair of both cartilage and subchondral bone.

4.1.3. Nanocomposite bioinks

Nanocomposite hydrogels are hydrogel systems formed by integrating a polymer matrix with nanoparticles or nanostructures. Although nanocomposite bioinks are often discussed as a broad material category, not all nanoparticles serve the same design purpose.[81] In osteochondral bioprinting, it is useful to distinguish between passive and active particle incorporation. Passive incorporation refers to particles that are added mainly to modify the surrounding hydrogel matrix, for example, by improving rheology and print fidelity, reinforcing mechanical properties, providing mineralising or lineage-directing cues, or introducing specialised bioactive functions.[82] Active incorporation, by contrast, refers to particles that participate more directly in network formation or structural organisation and therefore influence not only material properties but also gelation behaviour, degradation, and long-term construct stability.[83]

Recent extrusion-based studies from 2024 to 2026 further show that passive nanoparticle incorporation is not a single strategy, but a set of problem-specific tools. When the main limitation lies in rheology and print fidelity, nanoclay-type additives are primarily used as processing modifiers. For example, in a 2024 study on carboxymethyl cellulose (CMC)–laponite extrusion bioprinting, Corzo *et al.*[84] showed that increasing the laponite content in 1 wt% CMC bioinks markedly improved rheology and print fidelity during extrusion bioprinting. As the laponite content increased from 0 to 4 wt%, the consistency index rose from 0.101 to 304.12 $Pa{\cdot}s^n$, while the flow behaviour index decreased from 0.868 to 0.095. Correspondingly, laponite-containing inks achieved printability values of 0.9–1.0, whereas the laponite-free control remained below 0.7, and the 1C4L formulation exhibited the lowest diffusion rate and collapse factor. This improvement is consistent with the commonly proposed role of nanoclay particles that interact with multiple polymer chains, thereby increasing resistance to flow and supporting structural recovery after extrusion.[85] Importantly, the study also illustrated why biological readouts following extrusion should be interpreted alongside printing parameters. In the cell-laden dental pulp stem cell experiments, the authors reported using a 22-G conical needle, an extrusion

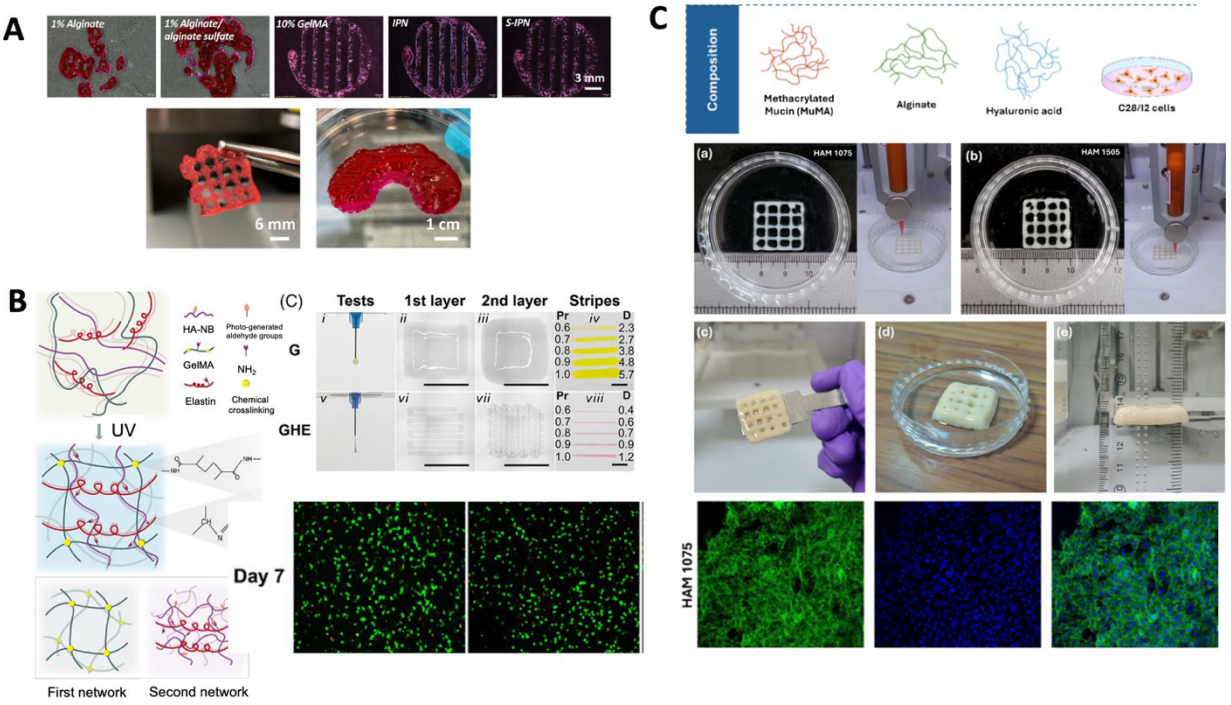

Figure 5. Interpenetrating network bioinks. (A) Printability of IPN bioinks, including defined printed hydrogel patterns, post-printing spreading ratio, shear-thinning coefficients, and representative 3D lattice and meniscus implant structures printed using S-IPN bioink. Scale bars: 3 mm, 6 mm, 1 cm. Adapted from Wang et al.[76] (B) Representative IPN/double-network systems showing hydrogel crosslinking mechanisms, printing optimisation, chondrocyte Live/Dead staining, and GelMA/silk fibroin composite IPN hydrogel fabrication for cartilage repair. Adapted from Wang et al.[78] (C) HAM-based IPN bioink synthesis and 3D bioprinting, including scaffold fabrication using HAM 1075 and HAM 1505 bioinks and cell proliferation/morphology analysis by phalloidin/Hoechst staining on day 14. Reprinted with permission from Sasikumar et al.[80] Copyright © 2025 American Chemical Society.
Abbreviations: GelMA: Methacrylate gelatine; HAM 1075: 15% (w/v) MuMA, 0.75% (w/v) hyaluronic acid, 1% (w/v) alginate, and 0.5% (w/v) LAP; HAM 1505: 15% (w/v) MuMA, 0.5% (w/v) hyaluronic acid, 1.5% (w/v) alginate, and 0.5% (w/v) LAP; IPN: Interpenetrating network; S-IPN: Sulphated IPN.

pressure of 22–25 kPa, a printing speed of 5 mm/s, and Live/Dead analysis after 48 h. However, although random fluorescence images were used to quantify live and dead cells, the spatial distribution of cells within the printed filament cross-section was not systematically analysed. Therefore, the reported cytocompatibility mainly supports short-term post-printing survival under the selected printing condition, rather than proving homogeneous cell distribution throughout the filament.

By contrast, some passively incorporated nanoparticles contribute less to extrusion itself than to post-printing reinforcement. Kosowska *et al.*[86] showed in 2024 that graphene oxide (GO) did not substantially improve the overall printability of an extrusion bioink. Nevertheless, GO-containing bioinks showed much lower swelling than their corresponding hydrogel controls. The swelling ratio decreased from 5,168% in HGO1 to 607% in BGO1, and from 3,329% in HGO2 to 513% in BGO2. However, this benefit was concentration-sensitive: BGO1 and BGO2 required approximately 20 and 30 kPa higher extrusion pressure than the reference bioink, and cell viability declined over time, with BGO2 falling to 61.6% at 48 h and BGO1 to 67.1% at 72 h. This makes the GO system a useful example of the need to separate material reinforcement from extrusion-associated cell stress. The decline in viability cannot be attributed solely to GO concentration or hydrogel chemistry, because the GO-containing formulations also required higher extrusion pressures. Without a corresponding analysis of nozzle geometry, shear or extensional stress, and cell distribution within printed filaments, Live/Dead or viability data may underestimate spatially localised cell damage caused by the printing process itself. In addition, some passively incorporated particles are introduced mainly to confer specialised post-printing responsiveness rather than simple reinforcement. Chakraborty *et al.*[87] incorporated anisotropic Fe_3O_4 magnetic nanoparticles at 5 mg/mL into a silk fibroin–gelatin extrusion bioink to generate shape-morphing magnetic constructs for cartilage regeneration (Figure 6A). The results showed that cyclic magnetic actuation for 30 min every other day promoted a more

favourable chondrogenic profile than shorter actuation or static controls. Specifically, it enhanced *SOX9*, *ACAN*, and *COL2A1* expression, reduced *COL10A1* and *MMP13*, and increased glycosaminoglycan and collagen deposition. Compared with studies that rely mainly on Live/Dead staining, this work provides a stronger functional assessment by linking the nanocomposite design to chondrogenic gene expression and matrix deposition. Nevertheless, its main focus was magnetic actuation and cartilage maturation rather than the influence of nozzle geometry on cell localisation during extrusion. Therefore, it supports the functional value of magnetic nanoparticles after printing, but it does not resolve whether cells were uniformly distributed across the printed filaments immediately after extrusion. These studies suggest that passively incorporated nanoparticles should be selected according to the dominant problem to be solved, whether that is improved extrusion, stronger post-printing support, or specialised functional responsiveness, rather than being treated as universally beneficial additives.

Active incorporation represents a conceptually distinct nanocomposite strategy because the particles no longer act solely as fillers but also as organising elements that participate directly in network formation or long-term structural stabilisation. A clear example is provided by Zengin *et al.*,[88] who used thiol-functionalised mesoporous silica nanoparticles as covalent crosslinking nodes in extrusion-printable norbornene-functionalised hydrogels (Figure 6B). This strategy tuned the gel mechanics from 9.3 to 19.7 kPa and introduced enzyme-responsive degradability via matrix metalloproteinase-sensitive surface modification. The resulting bioinks remained printable, preserved shape during culture, and supported the viability and proliferation of encapsulated MG63 cells. In their subsequent 2024 study,[89] the same design logic was extended to ECM-mimetic supramolecular fibrous hydrogels, where mesoporous silica nanoparticles functioned as covalent crosslinkers without disrupting the fibrous morphology. A related but broader perspective comes from Landau *et al.*,[90] who incorporated elastomeric poly(octamethylene maleate (anhydride) citrate) microparticles into natural hydrogels to counteract cell-driven compaction and swelling in 3D printed constructs. In their studies, the particles acted as mechanically functional structural elements rather than passive fillers. This enabled the bioink to retain the low-strain behaviour of the parent hydrogel while exhibiting greater resistance to deformation at larger strains and better long-term shape stability during tissue maturation. For these active nanocomposite systems, particle-mediated network formation may also change local stiffness, degradation, and transport at the microscale. Therefore, viability and proliferation assays should be complemented by analysis of particle dispersion, filament morphology, cell distribution, and matrix deposition, because uniformly printed constructs at the macroscale may still contain heterogeneous microenvironments at the cell scale.

Taken together, nanocomposite bioinks should be judged by the role the particles are intended to play within the construct. Passive incorporation is mainly useful for improving printability, mechanical support, or regional bioactivity, whereas active incorporation is more relevant for controlling network organisation and long-term structural behaviour. However, nanoparticle addition should not be evaluated only by filament fidelity, bulk mechanics, or endpoint Live/Dead staining. For cell-laden osteochondral constructs, it is also necessary to report nozzle and extrusion parameters, assess particle dispersion and filament-level cell distribution, and determine whether local heterogeneity affects matrix deposition, remodelling, and zone-specific tissue formation.

4.1.4. Supramolecular bioinks

Supramolecular bioinks are assembled through reversible noncovalent interactions, including host–guest binding, hydrogen bonding, metal coordination, hydrophobic association, and electrostatic interactions.[91] Unlike multimaterial, IPN, and nanocomposite bioinks, whose defining features are the addition of separate phases, independent networks, or particle reinforcement, these bioinks use reversible molecular recognition and bond exchange as the primary design principle. Recent reviews have emphasised that this design gives dynamic bioinks rapid stress relaxation, shear-thinning and self-healing behaviour, thereby improving cell–matrix communication, but also creates an inherent tension between microstructural dynamics and macroscopic stability. In other words, the distinctive value of supramolecular bioinks lies less in maximising bulk reinforcement than in introducing programmable post-printing adaptability into the matrix.

This adaptive role is supported by multiple studies focused on cartilage. In 2024, Dai *et al.*[92] showed that a supramolecular cartilage decellularised ECM (dECM) hydrogel (ECMCD) relaxed more than 80% of the initial stress within 1,000 s under a constant 15% strain, whereas the covalently crosslinked methacrylated dECM hydrogel (ECMMA) and ruthenium-crosslinked dECM hydrogel controls did not show comparable relaxation over the same period. Its viscosity also decreased from 156.3 to 0.7 Pa·s across the tested shear range, corresponding to an approximately 223-fold shear-thinning response. Biologically, adipose-derived stem cells migrated deeper into ECMCD within 7 days, most cells on ECMMA

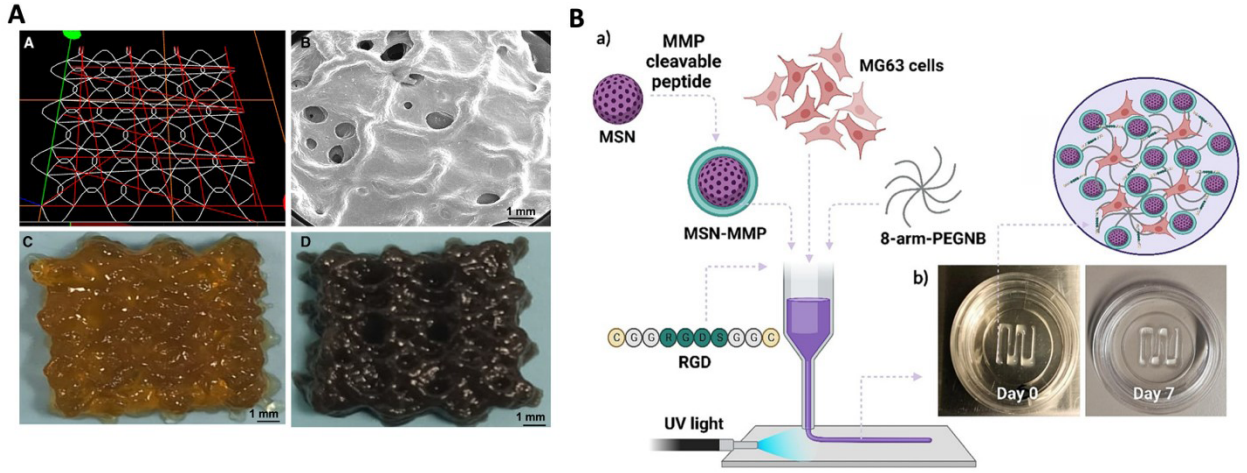

Figure 6. Nanocomposite bioinks. (A) Morphological analysis of bioprinted acellular constructs, including the G-code-designed printing pathway, field-emission scanning electron microscopy of the sinusoidal construct morphology, and optical images of constructs printed with or without magnetic nanoparticles. Scale bar: 1 mm. Adapted from Chakraborty *et al.*[87] (B) Mesoporous silica nanoparticle (MSN) bioinks for extrusion-based in situ bioprinting, showing the norbornene-modified 8-arm-PEG-20 K-MSN_2 hydrogel printing process and representative constructs on days 0 and 7. Adapted from Zengin *et al.*[88]

remained near the surface, and ECMCD further increased hypoxia-inducible factor 1-alpha expression by more than threefold over 14 days relative to ECMMA and ruthenium-crosslinked dECM hydrogel. Similarly, Xu *et al.*[93] reported that injectable host–guest macromer hydrogels carrying human BMSCs and chondrogenic factors improved osteochondral repair in rats: the Wakitani score decreased from 9.67 ± 1.86 and 9.50 ± 1.52 in GelMA controls to 3.83 ± 1.47 and 4.50 ± 1.52 in the injected supramolecular host–guest macromer groups loaded with kartogenin or TGF-β1, respectively. In another dual-dynamic hyaluronic acid/poly(γ-glutamic acid) system, Ma *et al.*[94] found that after 7 days, the DNA content in the highest-dynamic DN-3 formulation was nearly twofold that of the single-network control, while after 14 days, sulphated glycosaminoglycan and total collagen contents increased by approximately 1.5-fold and twofold, respectively. Taken together, these results indicate that supramolecular networks improve not only rheological adaptability but also cell migration, proliferation, and cartilage-specific matrix deposition after delivery.

A second advantage is that supramolecular design can couple matrix adaptability with active biological instruction. Ravi *et al.*[95] developed a hypoxia-mimicking supramolecular hydrogel by combining β-cyclodextrin-based host–guest assembly with cobalt nanowires and dexamethasone (Figure 7A). Relative to the control hydrogel, the storage modulus increased from 90 to 500 Pa, and the loss modulus from 30 to 120 Pa; in frequency sweeps, the elastic modulus increased from about 3,000 to 7,000 Pa and the viscous modulus from about 1,000 to 4,000 Pa. In parallel, hypoxia-mimicking supramolecular hydrogel significantly increased *HIF1A*, *COL2*, *ACAN*, and *SOX9* expression while decreasing *RUNX2* and *MMP13*, and histology showed greater Alcian blue, Safranin O, and toluidine blue staining over 7–21 days. The printed constructs also used defined extrusion parameters, including 10×10^6 umbilical cord MSCs mL^{-1}, a 20G needle, a printing speed of 10 mm s^{-1}, and 405 nm light at 10 mW cm^{-2} for 2 min after each layer. Beyond extrusion systems, Falandt *et al.*[96] showed in a hybrid supramolecular–covalent volumetric bioresin that host–guest modification improved shape fidelity sufficiently for self-supporting structures even at 40–60% degree of methacrylation, whereas equivalent covalent controls were less shape-retaining; hybrid gels also degraded more slowly, with low degrees of methacrylation covalent gels degrading completely within 45 min in collagenase, while all hybrid formulations persisted to 60 min. Together with increased MSC migration, vascular network formation, and organoid growth in the hybrid gels, these data suggest that supramolecular motifs can simultaneously encode biologically instructive and fabrication-relevant functions, rather than merely serving as passive rheology modifiers.

However, these advantages come at a clear trade-off: the same reversibility that enables cell-responsive remodelling may also limit long-term structural persistence. This is reflected in the way supramolecular motifs are increasingly

incorporated into mechanically stabilised hybrids rather than used as stand-alone load-bearing matrices. Stampoultzis *et al.*[97] introduced host–guest polyrotaxanes into a gelatin-based covalent matrix (Figure 7B). Although the bulk mechanical properties remained broadly comparable before cell encapsulation, and the storage modulus showed no significant difference from that of the covalent GelMA control, the dynamic formulations still enhanced chondrocyte mechanosensitivity. Specifically, *ACAN*, *PIEZO1,* and *TRPV4* increased by 30–200%, and under biomimetic thermomechanical stimulation, *ACAN* and *COL2A* were further upregulated by 200–250%. In a large-animal setting, Lewis *et al.*[98] showed that combining supramolecular peptide amphiphile filaments with crosslinked hyaluronic acid increased low-strain stiffness from 1.1 ± 0.2 to 5.0 ± 1.0 kPa relative to the peptide amphiphile/unmodified hyaluronic acid mixture, improved flow strain, reduced swelling, and supported significantly higher macroscopic appearance scores at 4 weeks in treated trochlear defects. By 12 weeks, the hybrid scaffold produced superior hyaline-like cartilage repair relative to growth factor-only controls in mechanically loaded sheep joints. More broadly, translational analyses of dynamic hydrogels now stress that bond exchange kinetics, mesh evolution, injectability, and long-term integrity are interdependent variables, not independently optimisable properties. Thus, supramolecular motifs appear to be most effective when used to add dynamic, cell-responsive behaviour to a stabilised framework rather than to replace structural support altogether.

Taken together, supramolecular bioinks are most distinctive not because they maximise structural reinforcement, but because they introduce quantifiably tunable, cell-responsive dynamics into printed matrices. Their greatest value in osteochondral bioprinting, therefore, emerges when stress relaxation, self-recovery, therapeutic retention, and cell-mediated remodelling are balanced against the need for long-term structural fidelity by complementary stabilising networks.

4.2. Biomimetic bone layer: Thermoplastics

4.2.1. Thermoplastics printed via fused deposition modelling

Thermoplastics are polymers that soften and become malleable upon heating and solidify upon cooling.

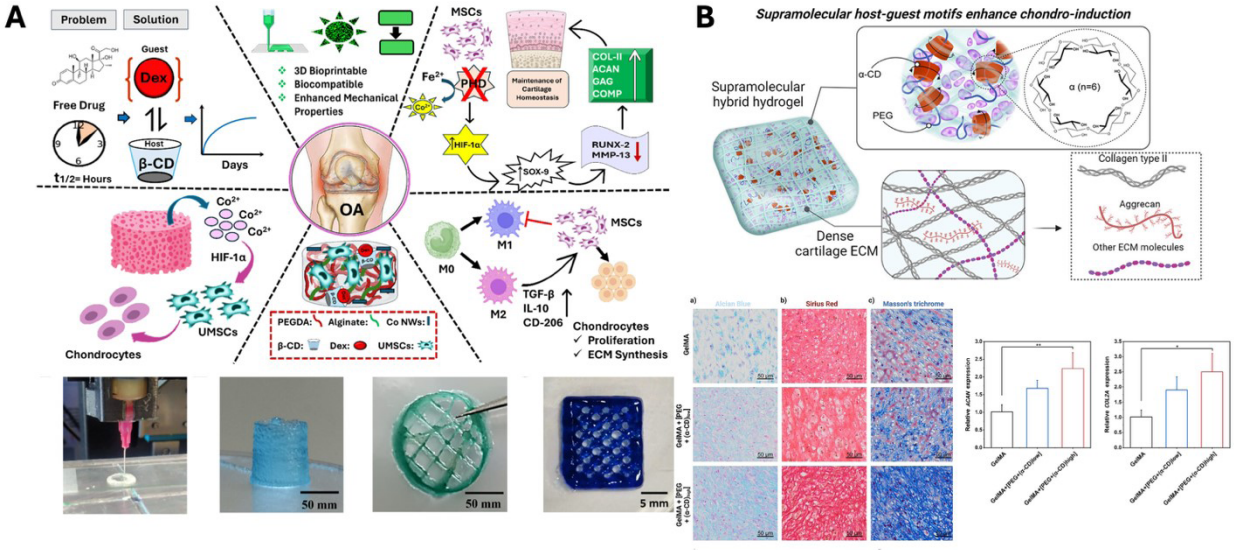

Figure 7. Supramolecular bioinks. (A) Schematic of a 3D-bioprintable hypoxia-mimicking supramolecular hydrogel for cartilage repair. Host–guest assembly between β-cyclodextrin and dexamethasone-containing guest polymers, together with cobalt nanowires, provides sustained therapeutic delivery, hypoxia-mimicking cues, and immunomodulatory function. Representative images show the bioprinting process and the printed cylindrical, circular, and rectilinear patterned constructs. Scale bars: 5 mm, 50 mm. Reprinted with permission from Ravi *et al.*[95] Copyright © 2025 American Chemical Society. (B) Supramolecular host–guest motifs enhance chondro-induction. The schematic illustrates a double-network supramolecular hybrid hydrogel designed to mimic the dynamic molecular nature of cartilage ECM. Representative histological images show (a) Alcian Blue staining for sulphated glycosaminoglycans and glycoproteins, (b) Sirius Red staining for collagen, and (c) Masson's trichrome staining for total collagen. Quantitative analysis shows relative ACAN and COL2A expression after thermomechanical stimulation. Scale bar: 50 μm; magnification: 20×. Adapted from Stampoultzis *et al.*[97]
Abbreviations: ACAN: Aggrecan; COL2A: Collagen type II; ECM: Extracellular matrix.

Their polymer chains are held together primarily by intermolecular forces, which weaken rapidly with increasing temperature, allowing the material to flow as a viscous melt. This reversible thermal behaviour makes thermoplastics particularly suitable for fused deposition modelling (FDM), enabling the fabrication of constructs with complex geometries.[99] For osteochondral scaffold design, however, printability alone is insufficient. The bone-layer material must also provide adequate mechanical support, degradation behaviour, osteoconductivity and architectural guidance for vascularised subchondral bone regeneration. Commonly used candidates include biodegradable polyesters such as poly(lactic acid) (PLA), PCL, poly(lactic-co-glycolic acid) (PLGA), and poly(hydroxyalkanoates) (PHA), as well as high-performance thermoplastics such as polyether ether ketone (PEEK) and related polyaryletherketones (Figure 8A).

Among common FDM-printable thermoplastics, their suitability depends on the balance between printability, degradation, and biological function. PCL or PLA/PCL blends are better suited for long-term structural support,[100] PLA- or PLGA-containing systems are useful when higher stiffness, faster degradation, or local delivery is required.[101] PHA-based materials offer biodegradable alternatives but remain less established in FDM-based osteochondral scaffolds,[102] and PEEK is mainly relevant when durable load-bearing fixation is prioritised.[103] Cheng *et al.*[104] provided a recent example of osteochondral tissue engineering by fabricating a polydopamine-modified triphasic PLA/PCL–PLGA/$Mg(OH)_2$ scaffold loaded with velvet antler polypeptides and fibrocartilage stem cells (Figure 8B). The PLA/PCL phase was used for the subchondral bone and dense osteochondral isolation layers, whereas PLGA/$Mg(OH)_2$ formed the cartilage-facing layer. The bone and cartilage layers were designed with pore sizes of 400 and 200 μm, respectively, and were processed by different routes: PLA/PCL was FDM-printed at 170 °C, while PLGA/$Mg(OH)_2$ was extruded at 10 °C. This layer-specific design shows that FDM thermoplastics are most effective when used as mechanically organised frameworks, while more degradable or bioactive phases are introduced to support cartilage-facing and interface functions.

Despite its versatility, FDM still has inherent limitations, including microstructural voids, dimensional inaccuracy, anisotropic mechanical behaviour, and weak interlayer adhesion, mainly caused by insufficient filament fusion. In osteochondral scaffolds, these defects may compromise load transfer across the cartilage–bone interface, reduce fatigue resistance, and cause non-uniform degradation or tissue ingrowth. Although printing parameters can be optimised to improve melt flow and interlayer bonding, excessive thermal exposure may accelerate polymer degradation or reduce reproducibility. Therefore, recent studies increasingly rely on composite, bioactive, or blended thermoplastic systems to improve both printability and scaffold function. Carbon-based fillers are useful for mechanical or electroactive reinforcement, whereas calcium phosphate-based fillers, such as hydroxyapatite, β-tricalcium phosphate (TCP), and bioactive glass, are more directly relevant to subchondral bone regeneration because they provide stiffness and osteoconductive cues. Wang *et al.*[100] demonstrated this using FDM-printed PCL/hydroxyapatite gyroid scaffolds (Figure 8C). As infill density increased from 40% to 60%, the compressive modulus increased from 46.6 to 71.6 MPa, within the reported cancellous bone range, while the 55% infill group showed the smallest water contact angle, a pore size of 465 ± 63 μm, cellular bridging, enhanced alkaline phosphatase activity, and calcium deposition. Bioactive polymer modification offers another strategy, as shown by Cantella *et al.*,[105] who developed a printable PCL–collagen peptide filament (Figure 8D). The collagen-containing PCL showed a tensile modulus of 536 ± 12 MPa, higher than lab-scale PCL alone, while maintaining printable triply periodic minimal surface architectures without visible sidewall voids, sagging, or poor layer adhesion; however, its compressive modulus was 227 ± 15 MPa, indicating that biofunctionalisation may improve tensile stiffness and printability without uniformly enhancing all mechanical properties. Polymer–polymer blending provides a further, but less recently emphasised, route to tune degradation and mechanical stability; however, polymer compatibility, phase separation, and mismatched degradation remain important concerns. Together, these studies suggest that FDM thermoplastic modification should be evaluated according to whether it improves structural support, osteoconductivity, degradation matching or interface stability, rather than printability alone.

Beyond filler incorporation and polymer blending, surface functionality and scaffold architecture are also critical considerations in FDM-based thermoplastic scaffold design. Surface characteristics such as hydrophilicity, roughness, and bioactivity regulate cell attachment and cell–material interactions, while pore architecture controls nutrient diffusion, vascular ingrowth, and spatial tissue organisation. Xu *et al.*[106] demonstrated the potential and limitations of bulk surface-functional modification by incorporating Ti_2AlN MXene into 3D-printed PCL scaffolds. Low MXene contents improved hydrophilicity, surface roughness, cell adhesion, and osteogenic activity, with the 5% Ti_2AlN/PCL group showing the highest cell proliferation and stronger alkaline phosphatase activity;

however, Ti_2AlN contents above 5% induced evident cytotoxicity, indicating that conductive or bioactive fillers require careful dose optimisation. At the architectural level, osteochondral scaffolds must also reproduce region-specific structural and biochemical cues. More directly for osteochondral repair, Wang *et al.*[107] combined an FDM-printed PCL framework with fast-degrading sodium alginate and slowly degrading silk fibroin to achieve sequential biomolecule delivery: E7 peptide was released rapidly to enhance BMSC migration within 72 h, whereas B2A peptide was released for more than 300 h to support later osteogenic and chondrogenic differentiation. This design demonstrates that FDM thermoplastic frameworks are most effective in osteochondral repair when they provide long-term mechanical support and spatial organisation, while hydrogel coupling or biomolecule delivery supplies region-specific biological cues.

Nevertheless, FDM-based printing remains constrained by the process's thermal requirements. The polymer must be heated above its melting or softening temperature to achieve sufficient flow for continuous extrusion, which

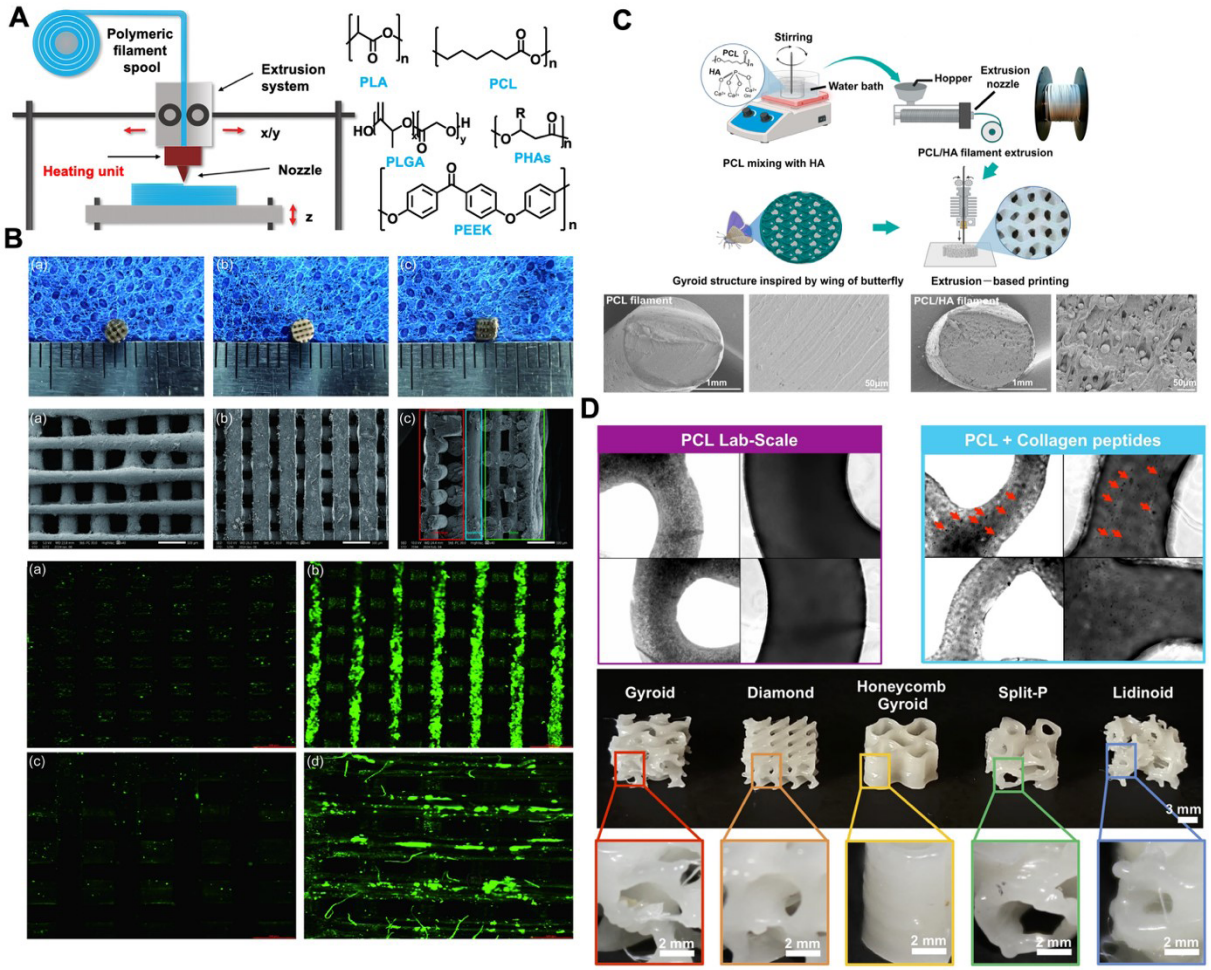

Figure 8. Thermoplastics printed via fused deposition modelling. (A) Schematic of fused deposition modelling (FDM) and representative thermoplastic polymers commonly processed by this method, including PLA, PCL, PLGA, PHAs, and PEEK. Adapted from Grivet-Brancot.[99] (B). Characterisation of a triphasic PLA/PCL–PLGA/$Mg(OH)_2$–VAP scaffold, showing gross morphology, layered pore architecture of the bone and cartilage regions, and VAP surface immobilisation visualised by fluorescence imaging. Scale bar: (a–c) 1 mm, (a–d) 500 μm. Adapted from Cheng *et al.*[104] (C) Filament fabrication and extrusion-based printing of PCL and PCL/HA composites, with representative schematics and scanning electron microscopy images of filament cross-sections and printed scaffold morphology. Scale bar: 1 mm, 50 μm. Adapted from Wang *et al.*[100] (D) Optical confirmation of collagen peptide incorporation in 3D-printed PCL-based filaments and representative TPMS scaffolds with different unit-cell geometries, including gyroid, diamond, honeycomb gyroid, split-P, and lidinoid. Scale bar: 2 mm. Adapted from Cantella *et al.*[105]

Abbreviations: HA: Hydroxyapatite; PCL: Poly(ε-caprolactone); PEEK: Polyether ether ketone; PHA: Poly(hydroxyalkanoates); PLA: Poly(lactic acid); PLGA: Poly(lactic-co-glycolic acid); TPMS: Triply periodic minimal surface; VAP: Velvet antler polypeptides.

limits the range of printable materials. This thermal requirement also prevents the direct encapsulation of living cells or temperature-sensitive biomolecules, making FDM less suitable for the cartilage-like or interface regions of osteochondral constructs. In addition, high-performance thermoplastics such as PEEK often require processing temperatures beyond the capabilities of many commercially available printers. Finally, FDM generally requires nozzle diameters greater than 150 μm, which limits the attainable feature size, printing resolution, and structural complexity of the final construct.[108] These limitations mean that FDM is better suited for printing the mechanically supportive bone phase than for fabricating the cell-rich cartilage phase or the fine biological interface between them.

4.2.2. Thermoplastics printed via solvent-cast direct writing

In solvent-cast direct ink writing (SC-DIW), the polymer is first dissolved in an organic solvent to form an ink. During extrusion, the solvent evaporates and leaves solid polymer filaments that are deposited layer by layer[109] (Figure 9A). Unlike FDM, SC-DIW can be performed at room temperature and is therefore suitable for polymers that are difficult to process thermally. In addition, several polymers commonly used in FDM for bone regeneration, including PCL, PLA, PLGA, and poly(L-lactic acid) (PLLA), can also be printed using this strategy. Dichloromethane (DCM) is one of the most commonly used solvents in SC-DIW.

Gu *et al.*[110] combined DIW with supercritical carbon dioxide foaming to prepare scaffolds with optimised pore structures (Figure 9B). In their study, PLGA was dissolved in a mixed solvent system consisting of DCM, 2-(2-butoxyethoxy)ethanol, and dibutyl phthalate, followed by the addition of hydroxyapatite to form the final ink. After carbon dioxide treatment, the P5H5-C group (PLGA/HA = 50:50) exhibited a more complex porous surface structure, thereby reducing stress concentration at filament junctions and improving scaffold permeability. Following cell seeding, the scaffolds promoted time-dependent rat BMSC proliferation, with the 800 μm pore size showing the most favourable effect. Polymer blending has also been explored to optimise SC-DIW inks. For example, Zhang *et al.*[111] developed a PLA/polyethene oxide ink using DCM as the solvent and further optimised the associated printing parameters. The incorporation of polyethene oxide also markedly improved scaffold hydrophilicity, making the constructs more suitable for osteogenic applications. Together, these studies show that solvent-based printing can expand the compositional and structural design space of thermoplastic scaffolds under mild conditions. However, they also illustrate an important processing trade-off. Although solvent-based printing enables the fabrication of porous, composite thermoplastic scaffolds under mild conditions, the use of mixed organic solvents, plasticisers, polymer blends, and high filler contents introduces additional variables that are rarely discussed in sufficient detail, including solvent evaporation kinetics, solvent–polymer interactions, and the possibility of residual solvent entrapment within thick or highly filled filaments. Therefore, improved porosity, permeability, or hydrophilicity should not be interpreted as sufficient evidence of biological suitability. For SC scaffolds, cytocompatibility depends not only on surface wettability and scaffold architecture, but also on the efficiency of solvent removal after printing. Quantitative assessment of residual solvent content, for example by gas chromatography or related analytical methods, should therefore be considered essential when evaluating SC-DIW scaffolds for bone or osteochondral repair.

Compared with FDM, SC-DIW also allows finer geometrical control. Tolbert *et al.*[112] dissolved PCL with different molecular weights in 1,1,1,3,3,3-hexafluoro-2-propanol (HFIP) and blended them at different ratios. The resulting scaffold had a filament diameter of 38.5 μm, a value difficult to achieve with FDM. By varying the proportion of PCL with different molecular weights, the authors investigated how mechanical cues influence human MSC behaviour under osteogenic and chondrogenic conditions without altering scaffold composition or architecture. Their results showed that lower-stiffness scaffolds supported more stable chondrogenic differentiation, whereas higher-stiffness scaffolds promoted hypertrophic cartilage formation and endochondral ossification. Nevertheless, the use of highly volatile and cytotoxic solvents such as HFIP raises a different concern. Even when cells are seeded after scaffold fabrication rather than printed directly within the ink, residual solvent may affect cell attachment, proliferation, differentiation, and inflammatory responses. This issue becomes particularly relevant for osteochondral applications, where scaffolds are often thick, porous, and compositionally heterogeneous, making complete solvent removal more difficult to guarantee.

In addition, SC-DIW can reduce excessive void formation often observed in FDM-printed scaffolds while enabling higher filler loadings, which may serve as rheological modifiers. Russias *et al.*,[113] for instance, used robotic deposition at ambient temperature to fabricate organic-inorganic hybrid scaffolds with precisely controlled microstructures. By dissolving PLA and PCL in DCM and incorporating hydroxyapatite, they obtained scaffolds with pore sizes ranging from 200 to 500 μm and a maximum hydroxyapatite content of 70 wt%. Such high ceramic

loading is advantageous for bone-like mineralisation and mechanical reinforcement, but it may also hinder solvent diffusion from the polymer matrix during drying. As a result, higher filler content may improve printability and bioactivity, but also increase the risk of local solvent retention. This dual effect should be explicitly considered when comparing SC-DIW with melt-based FDM.

Despite these advantages, solvent selection remains a major challenge in SC-DIW. The solvent must provide sufficient polymer solubility and appropriate flow behaviour while minimising toxicity and enabling controlled evaporation during mixing and extrusion. More importantly, residual solvent is not only a processing issue but also a translational barrier. This concern is supported by regulatory residual-solvent limits. According to the ICH Q3C(R9) guideline,[114] dichloromethane is classified as a Class 2 solvent and should be limited to a permitted daily exposure of 6.0 mg/day, corresponding to an Option 1 concentration limit of 600 ppm. Other solvents relevant to polymer scaffold processing also have defined limits, including N,N-dimethylformamide at 8.8 mg/day (880 ppm) and tetrahydrofuran at 7.2 mg/day (720 ppm). Although these limits were developed for pharmaceutical products rather than specifically for implanted 3D-printed scaffolds, they provide useful quantitative benchmarks for evaluating solvent-based scaffold fabrication.

Scaffold-related studies illustrate how such thresholds can be applied in practice. For example, residual DCM and N,N-dimethylformamide in PLGA/PCL electrospun membranes have been quantified by gas chromatography and compared directly with the. Food and Drug Administration/European Medicines Agency limits of 600 ppm and 880 ppm, respectively[115] (Figure 9C). This analysis is relevant to SC-DIW because both electrospinning and SC printing rely on polymer dissolution in organic solvents followed by post-fabrication solvent removal. In another study, residual HFIP retention was shown to depend strongly on polymer composition: pure gelatin fibres retained up to 1,600 ppm HFIP, whereas little HFIP or acetone was detected in 100% PCL fibres.[116] Vacuum plus heat treatment reduced HFIP to 10 ppm at 37 °C and 5.6 ppm at 45 °C, levels below those associated with reduced chondrocyte numbers in their toxicity test. The same study also showed that HFIP concentrations of 500 and 1,000 ppm significantly reduced chondrocyte numbers, whereas 100 and 250 ppm did not. These findings indicate that solvent residue cannot be inferred solely from solvent volatility, as polymer chemistry, scaffold thickness, porosity, filler content, and drying conditions may all influence solvent retention.

Many SC-DIW studies demonstrate short-term *in vitro* cytocompatibility after post-printing drying, vacuum treatment, or solvent exchange, but they do not always report residual solvent levels or compare them with accepted toxicological limits. Without such quantitative data, it is difficult to determine whether the observed biological response reflects the scaffold material itself or the combined effects of material composition, architecture, and residual processing solvent. Therefore, future SC-DIW studies should report solvent-removal protocols, residual solvent quantification, and cytotoxicity evaluation in a more standardised manner, particularly for scaffolds intended for *in vivo* implantation or clinical translation. Using less toxic or more easily removable solvents, optimising filament diameter and porosity, applying prolonged vacuum drying or supercritical carbon dioxide extraction, and verifying residual solvent content before biological testing may improve the translational credibility of this technique. In this sense, SC-DIW should not be viewed simply as a low-temperature alternative to FDM, but rather as a processing strategy whose benefits in terms of geometrical precision and material versatility must be balanced against solvent-related safety and regulatory concerns.

5. Interface design in hydrogel/thermoplastic osteochondral scaffolds

5.1. Importance of the interface

Having discussed hydrogels and thermoplastics separately, it is necessary to consider how these two distinct phases are integrated into one osteochondral construct. In native tissue, articular cartilage, calcified cartilage, and subchondral bone form a continuous transitional system rather than being defined by abrupt boundaries. However, many engineered osteochondral scaffolds still rely on simple bilayer designs, in which a soft hydrogel layer is directly combined with a rigid thermoplastic layer. Although easy to fabricate, such designs often fail to reproduce the structural continuity and functional coupling of the native osteochondral unit. The interface is therefore a key determinant of scaffold performance. Representative recent hydrogel/thermoplastic combination strategies for 3D-bioprinted osteochondral scaffolds are summarised in Table 1.

5.2. Major interface design strategies

Current interface strategies in hydrogel/thermoplastic osteochondral scaffolds can be understood as a progression from simple material juxtaposition to more integrated biomimetic designs. These strategies include direct bilayer or hierarchical multiphasic interfaces, gradient interfaces, calcified cartilage-mimetic intermediate layers, and geometrically interlocked interfaces. They differ not only

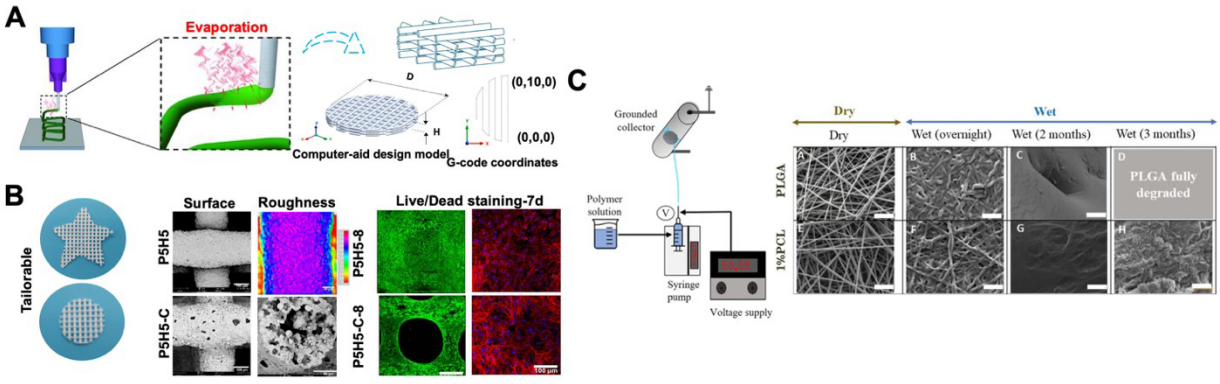

Figure 9. Thermoplastics printed via solvent-cast direct writing. (A) Schematic illustration of solvent evaporation during SC-DIW and computer-assisted design. Adapted from Balani *et al.*[109,111] (B) Tailorable properties of PLGA/HA scaffolds, showing representative scaffold morphologies, SEM images, ImageJ-based surface roughness reconstruction, and Live/Dead staining after 7 days of cell seeding. Scale bar: 40 μm, 100 μm, 400 μm. Reprinted with permission from Gu *et al.*[110] Copyright © 2022 American Chemical Society. (C) Fabrication and degradation behaviour of electrospun PLGA–PCL fibrous membranes. The schematic illustrates membrane manufacturing via electrospinning, and representative SEM images show that incorporating PCL delayed scaffold degradation under wet conditions (PBS at 37 °C) compared with plain PLGA. Scale bar: 10 μm. Adapted from Villanueva Navarrete *et al.*[115]
Abbreviations: HA: Hydroxyapatite; PBS: Phosphate-buffered saline; PCL: Poly(ε-caprolactone); PLGA: Poly(lactic-co-glycolic acid); SC-DIW: Solvent-cast direct ink writing; SEM: Scanning electron microscopy.

Table 1. Summary of three-dimensional bioprinted osteochondral scaffolds using hydrogel/thermoplastic combination strategy

Cartilage mimic layer	Calcified cartilage layer	Subchondral bone mimic layer	Cell type	Geometry/printing	Mechanical properties	Printability/ rheology	Ref.
Chondrocyte-laden GelMA + TA	PCL/nHA + TA	PCL	Rat primary chondrocytes; BMSCs; HUVECs	Three-layer cylindrical scaffold; diameter 2 mm, thickness 1.5 mm. PCL layer 1.0 mm / 10 layers; PCL-nHA layer 0.2 mm / 2 layers; GelMA layer 0.3 mm / 3 layers. PCL printed at 70 °C; GelMA bioink extruded at 21 °C; platform 21 °C; UV 3 mW cm^{-2} for 1 min; PCL nozzle 27G, 200 μm inner diameter	Porous PCL Young's modulus: 89.3 ± 8.74 MPa; PCL/nHA compressive modulus slightly higher than PCL, and tensile strength significantly higher	GelMA 5%, 10%, 15% tested. Viscosity measured from 0.01–1,000 s^{-1} at 25 °C. Higher GelMA concentration improved shear-thinning / shear-yielding and printability	Wu *et al.*, 2024[16]
Alg/HA/PEO hydrogel + Gel/PLGA short-cut fibres; best group: 25 wt% fibres	Comb-toothed interlocking interface formed by semi-immersion of PHG into hydrogel	PHG: 3D-printed PLGA/nHA framework filled with gelatine	BMSCs	PLGA 70 wt% + nHA 30 wt% dissolved/dispersed in DCM. Printing: barrel 20 °C, platform 45 °C, wire spacing 1.7 mm, extrusion pressure 0.45 MPa, speed 10 mm s^{-1}. PHG scaffold height 4 mm, diameter 5 mm; hydrogel thickness 2.3 mm; semi-immersion depth 0.3 mm	25 wt% short-cut fibres substantially enhanced mechanical integrity and promoted BMSC proliferation/ adhesion	Printable bone-layer parameters are explicit: 0.45 MPa extrusion pressure, 10 mm s^{-1} speed, 20/45 °C barrel/ platform	Liu *et al.*, 2025[117]

(*cont'd...*)

Table 1. (*Continued*)

Cartilage mimic layer	Calcified cartilage layer	Subchondral bone mimic layer	Cell type	Geometry/printing	Mechanical properties	Printability/ rheology	Ref.
TPU scaffold filled with gelatine: TPU/ Gel	N/A	PLA/HA	Chondrocytes, osteoblasts, and BMSCs in assays	FDM-printed bilayer scaffold. Fibre diameter 500 μm, fibre spacing 500 μm, porosity 30%	Compression modulus / E values: TPU: 1.079 ± 0.031 MPa; TPU + PLA: 13.620 ± 1.143 MPa; TPU + PLA/HA: 21.336 ± 3.683 MPa; PLA: 38.210 ± 3.853 MPa; PLA/HA: 44.369 ± 2.515 MPa. Interfacial shear strength: PLA: 1.359 ± 0.019 N; TPU: 0.673 ± 0.051 N; TPU + PLA: 0.843 ± 0.052 N; PLA/ HA: 0.576 ± 0.067 N; TPU + PLA/HA: 0.73 ± 0.027 N	FDM-printable thermoplastic scaffold; gelatin filling after printing	Wang *et al.*, 2025[118]
GelMA/BC@ PLLAms; BC-loaded PLLA microspheres in GelMA	N/A	Cur@TCP-PCL-PEG	MC3T3-E1; chondrocytes; BMSCs	Low-temperature 3D printing. Lower Cur@TCP-PCL-PEG layer printed first; at 50% completion, the cartridge switched to GelMA/BC@ PLLAms to complete the bilayer scaffold. The interface showed no obvious cracks	Compression tested on 6.5 × 7.5 × 5 mm samples; strain set to 80%, load 1 kN, loading rate 0.5 mm min^{-1}. Cur@ TCP-PCL-PEG had highest compressive strength; bilayer scaffold intermediate; GelMA/BC@ PLLAms lowest	Both GelMA/ BC@PLLAms and Cur@TCP-PCL-PEG inks showed shear-thinning. Storage modulus G′ and loss modulus G″ decreased with increasing strain and intersected, supporting printability and post-print shape retention	Gu *et al.*, 2026[119]
PLA/PCL-based upper/ cartilage-related layer with VAP functionalisation	PLGA/ $Mg(OH)_2$-related middle/ interfacial component	PLA/PCL or PLGA/ $Mg(OH)_2$-based scaffold component	Not primarily cell-laden; focuses on VAP-functionalised scaffold bioactivity	Surface modification: scaffold immersed in polydopamine solution for 8 h; EDC/NHS activation with 208 mg EDC + 136 mg NHS in 10 mL MES; VAP immobilised overnight	Compressive modulus: cartilage layer: 20.7086 ± 0.63024 MPa; bone layer: 65.5044 ± 1.98451 MPa	Low-temperature extrusion printing for the PLGA/ $Mg(OH)_2$ cartilage layer at 10 °C with 200 μm pores; FDM printing for the PLA/PCL bone and dense isolation layers at 170 °C with 400 μm bone-layer pores; rheological parameters were not reported	Cheng *et al.*, 2024[104]

Abbreviations: Alg: Alginate; BC: Bacterial cellulose; BMSCs: Bone marrow mesenchymal stem cells; Cur: Curcumin; DCM: Dichloromethane; EDC: 1-Ethyl-3-(3-dimethylaminopropyl)carbodiimide; FDM: Fused deposition modelling; Gel: Gelatine; GelMA: Gelatin methacryloyl; HA: Hydroxyapatite; HUVECs: Human umbilical vein endothelial cells; MC3T3-E1: Mouse calvaria-derived preosteoblast cell line MC3T3-E1; MES: 2-(N-morpholino) ethanesulfonic acid; MPa: Megapascal; nHA: Nano-hydroxyapatite; NHS: N-Hydroxysuccinimide; PBS: Phosphate-buffered saline; PCL: Poly(ε-caprolactone); PEG: Polyethylene glycol; PEO: Polyethylene oxide; PHG: PLGA/nHA framework filled with gelatine; PLA: Poly(lactic acid); PLGA: Poly(lactic-co-glycolic acid); PLLAms: Poly(L-lactic acid) microspheres; TA: Tannic acid; TCP: Tricalcium phosphate; TPU: Thermoplastic polyurethane; UV: Ultraviolet; VAP: Velvet antler polypeptides.

in fabrication complexity but also in their ability to address the mechanical mismatch and biological discontinuity between cartilage-like and bone-like phases.

The simplest strategy is the direct bilayer interface, in which a hydrogel phase is deposited directly onto or within a thermoplastic framework. This approach is attractive because of its simplicity and compatibility with sequential bioprinting workflows. It also allows each phase to be optimised independently for its target tissue. However, direct bilayer interfaces often result in sharp transitions in modulus, pore architecture, and degradation behaviour. This may lead to stress concentration, poor force transfer, and interfacial instability. Recent bilayer and hierarchical multiphase scaffolds demonstrate that interface stability is increasingly being considered an explicit design target. For example, Ghorbani *et al.*[120] developed a PCDE scaffold consisting of a 3D-printed polydopamine-modified PCL phase, an electrospun PCL-gelatin layer, and an immobilised gelatin-BMP-2 coating (Figure 10A). The multi-phasic PCDE scaffold exhibited higher mechanical performance than the PC and mono-phasic PCD scaffolds. Specifically, its compressive strength was reported to be 1.9- and 1.7-fold higher than those of the PC and PCD scaffolds, respectively, while its compressive modulus was 2.1- and 2.2-fold higher, respectively. The authors also reported enhanced interfacial bonding between the electrospun and 3D-printed layers, indicating improved interlayer integrity.[120] Similarly, Gu *et al.*[119] reported a GelMA/bacterial cellulose@Poly(L-lactic acid) microspheres–curcumin@TCP-PCL-PEG bilayer scaffold with an intermingled interface and no obvious cracks. Mechanical testing showed that the bilayer scaffold exhibited compressive strength and Young's modulus values intermediate between those of the soft GelMA/bacterial cellulose@Poly(L-lactic acid) microspheres layer and the rigid curcumin@TCP-PCL-PEG layer, indicating that the bilayer design retained mechanical support while incorporating a softer cartilage-oriented phase.[119] However, these studies still mainly demonstrate improved layered integration rather than a continuous osteochondral transition or a fully calcified cartilage-mimetic barrier.

A more advanced strategy is the gradient interface, in which compositional, structural, or mechanical properties change progressively across the osteochondral depth. This design is closer to native osteochondral tissue, where cartilage, calcified cartilage, and subchondral bone form a gradual transition rather than an abrupt boundary. In extrusion-based systems, such gradients can be generated by controlling ink composition, mineral content, crosslinking density, bioactive cues, or filament arrangement during printing. Mahajan *et al.*[121] developed extrusion-fabricated CMC–silk IPN hydrogels with opposing biochemical gradients. The base hydrogel contained 1% w/v methacrylated CMC, 5% w/v methacrylated silk, and 0.4% w/v lithium phenyl-2,4,6-trimethylbenzoylphosphinate. The cartilage-specific formulation contained 1% w/v sulphated CMC and 1 μg mL^{-1} TGF-β1, whereas the bone-specific formulation contained 30% w/w hydroxyapatite. The gradient was mainly demonstrated by compositional mapping rather than mechanical testing: toluidine blue staining and sulphur energy-dispersive X-ray spectroscopy mapping showed higher sulphated CMC in the cartilage-like region; immunofluorescence intensity profiling showed a TGF-β1 gradient; and calcium/phosphate mapping, together with micro-computed tomography, confirmed hydroxyapatite enrichment toward the bone-like region. Wu *et al.*[33] further used dual-nozzle cross-printing and gradient crosslinking to fabricate a heterogeneous bilayer hydrogel scaffold. The upper layer contained sodium alginate and decellularised natural cartilage, whereas the lower layer contained sodium alginate, GelMA, and nano-hydroxyapatite (nHA). Cross-printing in the transitional region produced a calcification-like layer, and subsequent $CaCl_2$ and ultraviolet crosslinking were used to reduce delamination. The optimised G-decellularised natural cartilage/nHA scaffold showed close adhesion between the two layers, no distinct boundary under scanning electron microscopy, and a compressive modulus of 94.64 ± 5.27 kPa, higher than the control scaffold at 70.55 ± 4.29 kPa. More directly, Zhao *et al.*[122] reported a one-step bioextrusion strategy to generate an agarose-based osteochondral graft with a continuous hydroxyapatite gradient from 0% to 20%. The measured gradient length was 647 ± 21 μm, close to that of native bovine osteochondral tissue, and the graft maintained structural integrity during compression and stress relaxation testing. Together, these studies show that extrusion-based gradient interfaces can provide spatially organised biochemical and mineral cues and may reduce abrupt discontinuity between cartilage-like and bone-like regions.

A related but more functionally specific strategy is the incorporation of a calcified cartilage-mimetic intermediate layer. While gradient interfaces mainly smooth compositional or mechanical transitions, this approach aims to reproduce the specialised barrier role of native calcified cartilage. Native calcified cartilage is a thin but mechanically distinct region, with a reported thickness of 104.16 ± 20.87 μm, compressive modulus of 208.6 ± 39.7 MPa, and tensile modulus of 178.3 ± 35.9 MPa.[123] For example, Wu *et al.*[16] developed a 3D-printed biomimetic osteochondral scaffold containing a compact nHA–PCL interfacial layer loaded with tasquinimod

between the cartilage-like and bone-like regions. In this design, tasquinimod was incorporated not as a mechanical reinforcing component, but as an anti-angiogenic cue to inhibit vascular invasion into the cartilage-like layer and help preserve the avascular cartilage microenvironment. The nHA particles were 200–500 nm in length and 20–30 nm in diameter, and their incorporation into PCL produced a compact mineralised interface. The porous PCL scaffold showed a Young's modulus of 89.3 ± 8.74 MPa, while the PCL–nHA interfacial layer showed a slightly higher modulus. More importantly, tasquinimod release from the PCL-nHA layer was sustained, reaching approximately 40% over two weeks, whereas release from the GelMA layer was nearly complete over the same period. This sustained local release helped suppress vascular invasion into the cartilage region and supported the barrier-like function of the calcified interface. Therefore, the study demonstrates that a calcified cartilage-mimetic layer should be evaluated not only by mineral content or mechanical continuity, but also by its ability to maintain cartilage–bone compartmentalisation over time. Wang *et al.*[124] further extended this concept by using a triphasic hybrid construct in which a co-printed GelMA/PCL–TCP calcified layer served simultaneously as a transition zone, bonding interface, and a directional cell-release layer (Figure 10B). Quantitatively, the triphasic construct reached a compressive modulus of about 190 kPa, and interlocking increased the maximum separation force from ~0.42 to ~0.73 N. Functionally, human adipose-derived stem cells were released from the calcified layer towards the PCL/TCP bone region by day 14, whereas upward migration into the methacrylated methylcellulose/GelMA cartilage layer was restricted, supporting the role of the calcified layer in both structural integration and biological compartmentalisation.

More recently, increasing attention has been directed towards geometrically interlocked interfaces. In these designs, the cartilage-like hydrogel and bone-like scaffold are connected through physical interpenetration rather than simple planar stacking. Liu *et al.*[117] provided a representative example by combining a short-cut fibre-reinforced sodium alginate/hyaluronic acid hydrogel with a 3D-printed PLGA/nHA/gelatin scaffold. During fabrication, the bone scaffold was partially immersed in the hydrogel by 0.3 mm, followed by $CaCl_2$ and 1-ethyl-3-(3-dimethylaminopropyl)carbodiimide/N-

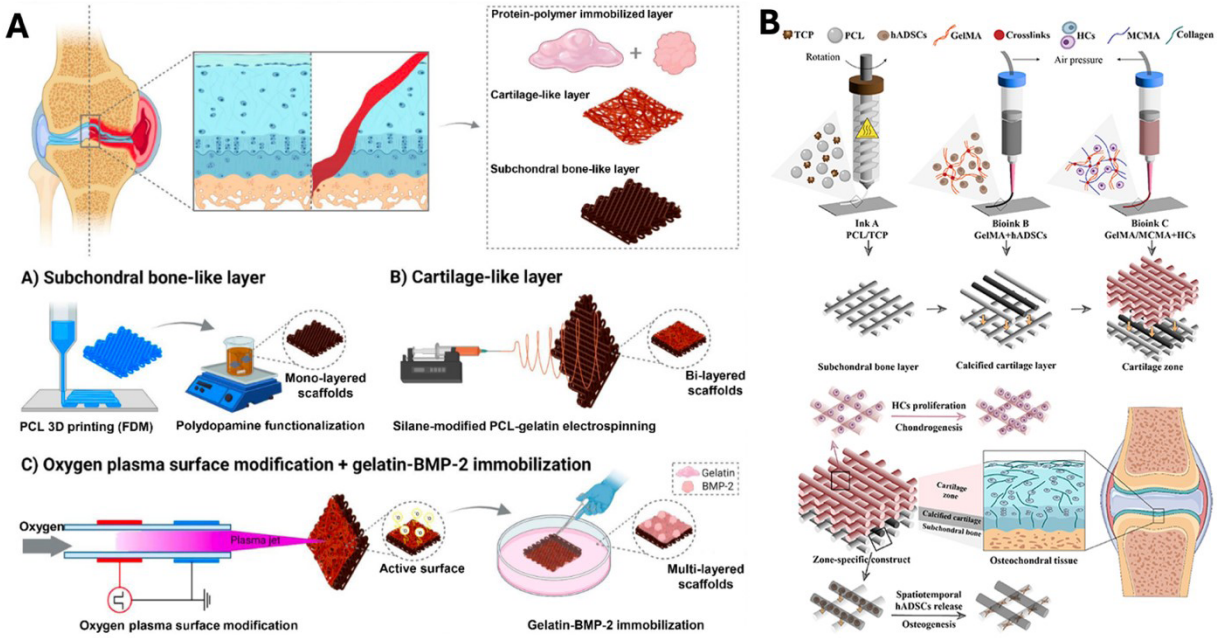

Figure 10. Thermoplastic/hydrogel bioprinting design. (A) Sequential fabrication of a multiphasic scaffold for osteochondral regeneration, including a polydopamine-functionalised PCL subchondral bone-like layer, an electrospun PCL–gelatin cartilage-like layer, and gelatin–BMP-2 immobilisation after oxygen plasma treatment. Adapted from Ghorbani et al.[120] (B) One-step hybrid 3D bioprinting of a triphasic osteochondral construct composed of a PCL/TCP subchondral bone region, a co-printed GelMA/hADSC–PCL/TCP calcified cartilage layer, and an MCMA/GelMA/HC cartilage region. Adapted from Wang et al.[124]

Abbreviations: BMP-2: Bone morphogenetic protein-2; GelMA/hADSC: Methacrylated gelatin/human adipose-derived stem cell; MCMA/GelMA/HC: Methacrylated methylcellulose/methacrylated gelatin/human chondrocytes; PCL: Polycaprolactone; PCL/TCP: Polycaprolactone/tricalcium phosphate.

hydroxysuccinimide crosslinking, which allowed the hydrogel to penetrate the grooves of the printed scaffold and form a comb-toothed interlocking structure. The hydrogel layer was further reinforced with 25% short-cut gelatin/PLGA fibres, increasing its wet compressive stress at 80% strain from 0.057 MPa to 0.102 MPa compared with the fibre-free hydrogel. This design therefore improved the mechanical properties of the cartilage-like phase by using geometric interlocking to anchor it to the bone-like scaffold. *In vivo*, the PLGA/nHA/gelatin/AHPF scaffold produced smoother and thicker cartilage repair and more continuous subchondral bone formation after 12 weeks. However, the study did not directly quantify interfacial shear or peel strength. Therefore, it supports the potential of interlocking interfaces but also highlights the need for more systematic mechanical testing of interface stability.

Overall, these interface strategies show that successful osteochondral scaffold design should not focus solely on the properties of the cartilage-like and bone-like phases. Equal attention should be given to how these phases are connected, how mechanical loads are transferred across the construct, and how zonal biological functions are maintained over time.

6. Conclusion and future outlook

Hydrogel/thermoplastic osteochondral scaffolds have progressed from simple bilayer constructs towards more biomimetic, mechanically integrated, and biologically instructive systems. By combining the hydrated, cell-permissive features of hydrogels with the mechanical support and architectural stability of thermoplastics, these hybrid scaffolds provide a versatile platform for reconstructing the cartilage–bone unit. Nevertheless, their clinical translation remains limited not only by biological performance, but also by practical issues related to regulatory classification, manufacturing reproducibility, sterilisation, residual solvent control, and cost-effective scale-up.

From a regulatory perspective, these scaffolds do not fit into a single simple category. Acellular thermoplastic-supported constructs may be considered closer to medical devices and, depending on the risk profile and predicate availability, may follow device-oriented pathways such as 510(k), *de novo*, or premarket approval. By contrast, cell-laden, growth-factor-loaded, or drug-eluting scaffolds may require evaluation as biologics or combination products. For additively manufactured medical devices, the Food and Drug Administration has emphasised that design control, material control, post-processing, process validation, acceptance testing, dimensional assessment, material characterisation, removal of manufacturing residues, sterilisation, and biocompatibility should all be considered during development.[125] Therefore, future osteochondral scaffold design should become more "regulatory-aware," with material selection and fabrication routes chosen not only for regenerative efficacy but also for compatibility with realistic approval pathways, quality systems, and release criteria.

Manufacturing readiness is another major bottleneck. In particular, solvent-assisted approaches such as SC-DIW require careful control of residual solvents. The use of volatile organic solvents can enable low-temperature printing of thermoplastics, but solvent removal should not be assumed to occur solely through drying or lyophilisation. Instead, residual solvents should be quantified, ideally by headspace gas chromatography–mass spectrometry or gas chromatography–flame ionisation detection, and discussed against recognised safety limits. According to ICH Q3C, residual solvents should be removed as far as possible because they provide no therapeutic benefit, and Class 2 solvents should be limited to protect patients from potential adverse effects.[114] This is particularly relevant for solvents commonly used in scaffold fabrication, such as dichloromethane, tetrahydrofuran, and 1,4-dioxane. Future SC-DIW studies should therefore report residual solvent levels together with cytotoxicity, extractables/leachables testing, and scaffold mechanical performance, rather than treating solvent evaporation as a purely technical processing step.

Sterilisation is equally important but remains under-discussed in many osteochondral scaffold studies. From a translational perspective, steam sterilisation deserves particular attention because it is a clinically established, residue-free, and widely implemented sterilisation process. However, its suitability for hydrogel/thermoplastic osteochondral scaffolds cannot be assumed. Hydrogel/thermoplastic composites are especially challenging because the hydrogel phase may undergo changes in swelling, crosslinking density, or bioactivity, whereas the thermoplastic phase may experience changes in molecular weight, crystallinity, degradation rate, or mechanical strength after the same sterilisation treatment. For steam sterilisation specifically, exposure to high temperature, pressure, and moisture may alter hydrogel network integrity, swelling behaviour, crosslinking density, and bioactivity, while also affecting thermoplastic crystallinity, dimensional stability, degradation behaviour, and mechanical strength. These effects are particularly important in multiphasic osteochondral constructs, where the cartilage-like hydrogel phase, bone-like thermoplastic phase, and interfacial region may respond differently to the same sterilisation cycle.

Alternative low-temperature or non-steam methods, including ethylene oxide, gamma irradiation, electron beam sterilisation, and supercritical carbon dioxide, may be considered when steam sterilisation is incompatible with temperature-sensitive or bioactive scaffold components. However, these methods should be treated as material- and process-dependent alternatives rather than default translational solutions, because they may introduce residual toxicity, radiation-induced chain scission or crosslinking, dose-dependent degradation, or changes in swelling, porosity, and interfacial bonding. Thus, sterilisation should be considered part of scaffold design rather than a final downstream step. Future studies should evaluate the scaffold before and after sterilisation with respect to chemistry, pore structure, swelling, degradation, mechanical properties, interfacial strength, and biological response.

Scale-up manufacturing, product purity, impurity profiling, and chemical analysis, such as extractables and leachables testing, also require greater attention. Product purity is important for clinical translation because even small amounts of residual chemicals may affect safety and performance. These impurities may include residual solvents, unreacted monomers, crosslinkers, photoinitiators, catalysts, degradation products, endotoxins, and leachable additives. They may reduce cell viability, trigger inflammation, interfere with tissue regeneration, or raise regulatory concerns. Many reported hydrogel/thermoplastic scaffolds are produced at the laboratory scale. At this scale, printing fidelity, phase distribution, crosslinking, drying, environmental contamination, and storage are difficult to control and minimise across batches. Purity control is especially challenging in hydrogel/thermoplastic composites because each phase may introduce different impurities. The hydrogel phase may retain residual crosslinkers, photoinitiators, or unreacted macromers. The thermoplastic phase may contain residual organic solvents, plasticisers, processing additives, or low-molecular-weight degradation products. Additional components, such as nanoparticles, growth factors, or surface-functionalised molecules, can further complicate impurity profiling and release testing. Therefore, extractables and leachable analysis, residual solvent quantification, endotoxin testing, and batch-to-batch chemical characterisation should be included early in scaffold development. They should not be treated only as late-stage regulatory requirements.

This issue becomes more serious for gradient, interlocking, patient-specific, or cell-laden constructs. Although such designs may provide stronger biomimicry, their translational value will be limited if they require complex multi-step fabrication, expensive bioactive factors, autologous cells, difficult storage, or prolonged post-processing or purification steps. Future studies should therefore evaluate not only whether a scaffold can regenerate osteochondral tissue under ideal experimental conditions, but also whether it can be manufactured reproducibly, meet predefined purity and impurity specifications, be sterilised safely, be stored and transported reliably, and be implanted at a clinically acceptable cost. Simple health-economic or cost–benefit considerations should be incorporated when advanced architectures, autologous cells, or multiple bioactive factors are proposed.

Future progress should therefore move from material-centred optimisation towards translation-centred integration. First, standardised evaluation frameworks are needed, including bulk mechanical testing, interfacial shear or tensile strength, fatigue resistance, residual solvent analysis, sterilisation compatibility, degradation behaviour, and spatially resolved tissue integration. Secondly, scaffold concepts should be stratified according to translational intent: acellular off-the-shelf scaffolds, cell-laden personalised constructs, and bioactive combination products each face different regulatory and manufacturing barriers. Thirdly, interface design should be developed according to regulatory-compliant manufacturing and sterilisation strategies, because an elegant gradient or interlocking architecture may fail if post-processing weakens the interface or changes the hydrogel/thermoplastic balance. Finally, more long-term large-animal studies under clinically relevant loading conditions are needed to determine whether these scaffolds can maintain mechanical integrity, biological integration, and functional repair over time.

In summary, hydrogel/thermoplastic osteochondral scaffolds offer a promising route towards integrated cartilage and bone regeneration, but their future impact will depend on more than increasing structural complexity. The next stage of the field should prioritise scaffolds that are not only biomimetic and biologically active, but also manufacturable, sterilisation-compatible, reproducible, cost-conscious, and aligned with realistic clinical translation pathways.

Abbreviation list

Abbreviation	Full term
3D	Three-dimensional
ACAN	Aggrecan
BC	Bacterial cellulose
BGO	Graphene oxide-containing bioink group

(cont'd...)

(Continued)

BMSC/BMSCs	Bone marrow mesenchymal stem cell(s)
$CaCl_2$	Calcium chloride
CMC	Carboxymethyl cellulose
CT	Computed tomography
Cur	Curcumin
dECM	Decellularised extracellular matrix
DIW	Direct ink writing
DN	Double network
dNC	decellularised natural cartilage
ECM	Extracellular matrix
ECMCD	Supramolecular cartilage decellularised extracellular matrix hydrogel
ECMMA	Methacrylated decellularised extracellular matrix hydrogel
FDM	Fused deposition modelling
GelMA	Gelatin methacrylate / methacrylated gelatin
GO	Graphene oxide
G′	Storage modulus
G″	Loss modulus
HAM	Hyaluronic acid-alginate-mucin formulation
HFIP	1,1,1,3,3,3-hexafluoro-2-propanol
IPN/IPNs	Interpenetrating network(s)
$Mg(OH)_2$	Magnesium hydroxide
MSC/MSCs	Mesenchymal stem cell(s)
nHA / nano-HA	Nano-hydroxyapatite
OCT3/4	Octamer-binding transcription factor 3/4
PCL	Polycaprolactone / poly(ε-caprolactone)
PEEK	Polyether ether ketone
PEG	Polyethylene glycol
PEO	Polyethylene oxide
PHA	Poly(hydroxyalkanoates)
PHG	PLGA/nHA/gelatin scaffold
PLA	Poly(lactic acid)
PLGA	Poly(lactic-co-glycolic acid)
PLLA	Poly(L-lactic acid)
PLLAms	Poly(L-lactic acid) microspheres
POMaC	Poly(octamethylene maleate citrate)
SC-DIW	Solvent-cast direct ink writing
TCP / β-TCP	Tricalcium phosphate / beta-tricalcium phosphate
TGF-β1	Transforming growth factor beta 1
TGF-β3	Transforming growth factor beta 3
Ti_2AlN	Titanium aluminium nitride MXene
TPMS	Triply periodic minimal surface
TPU	Thermoplastic polyurethane
VAP	Velvet antler polypeptide

Acknowledgments

None.

Funding

This work was funded by the University of Leeds-China Scholarship Council (CSC) Joint Scholarship (No. 202206220017).

Conflict of interest

The authors declare they have no competing interests.

Author contributions

Conceptualization: Mingzu Du, David J. Wood
Supervision: Giuseppe Tronci, Xuebin B. Yang, David J. Wood
Visualization: Mingzu Du
Writing–original draft: Mingzu Du
Writing–review & editing: Giuseppe Tronci, Xuebin B. Yang, David J. Wood

Ethics approval and consent to participate

Not applicable.

Consent for publication

Not applicable.

Availability of data

Not applicable.

References

1. Wei W, Dai H. Articular cartilage and osteochondral tissue engineering techniques: Recent advances and challenges. *Bioact Mater*. 2021;6(12):4830-4855.

   doi: 10.1016/j.bioactmat.2021.05.011

2. Komarraju A, Goldberg-Stein S, Pederson R, McCrum C, Chhabra A. Spectrum of common and uncommon causes of knee joint hyaline cartilage degeneration and their key imaging features. *Eur J Radiol*. 2020;129:109097.

   doi: 10.1016/j.ejrad.2020.109097

3. Ai C, Lee YHD, Tan XH, Tan SHS, Hui JHP, Goh JC-H. Osteochondral tissue engineering: perspectives for clinical application and preclinical development. *J Orthop Transl*. 2021;30:93-102.

doi: 10.1016/j.jot.2021.07.008

4. Ji S, Guvendiren M. Recent advances in bioink design for 3D bioprinting of tissues and organs. *Front Bioeng Biotechnol*. 2017;5:23.

   doi: 10.3389/fbioe.2017.00023

5. Chen W, Xu Y, Li Y, *et al*. 3D printing electrospinning fiber-reinforced decellularized extracellular matrix for cartilage regeneration. *Chem Eng J*. 2020;382:122986.

   doi: 10.1016/j.cej.2019.122986

6. Badar W, Inamdar SR, Fratzl P, *et al*. Nonlinear Stress-Induced Transformations in Collagen Fibrillar Organization, Disorder and Strain Mechanisms in the Bone-Cartilage Unit. *Adv Sci*. 2025;12(1):2407649.

   doi: 10.1002/advs.202407649

7. Lee JM, Suen SKQ, Ng WL, Ma WC, Yeong WY. Bioprinting of collagen: considerations, potentials, and applications. *Macromol Biosci*. 2021;21(1):2000280.

   doi: 10.1002/mabi.202000280

8. Chartrain NA, Gilchrist KH, Ho VB, Klarmann GJ. 3D bioprinting for the repair of articular cartilage and osteochondral tissue. *Bioprinting*. 2022;28:e00239.

   doi: 10.1016/j.bprint.2022.e00239

9. Dhawan A, Kennedy PM, Rizk EB, Ozbolat IT. Three-dimensional bioprinting for bone and cartilage restoration in orthopaedic surgery. *J Am Acad Orthop Surg*. 2019;27(5):e215-e226.

   doi: 10.5435/JAAOS-D-17-00632

10. Ozbolat IT, Hospodiuk M. Current advances and future perspectives in extrusion-based bioprinting. *Biomaterials*. 2016;76:321-343.

    doi: 10.1016/j.biomaterials.2015.10.076

11. Kesti M, Müller M, Becher J, *et al*. A versatile bioink for three-dimensional printing of cellular scaffolds based on thermally and photo-triggered tandem gelation. *Acta Biomater*. 2015;11:162-172.

    doi: 10.1016/j.actbio.2014.09.033

12. Chiulan I, Frone AN, Brandabur C, Panaitescu DM. Recent advances in 3D printing of aliphatic polyesters. *Bioengineering*. 2017;5(1):2.

    doi: 10.3390/bioengineering5010002

13. Hölzl K, Lin S, Tytgat L, Van Vlierberghe S, Gu L, Ovsianikov A. Bioink properties before, during and after 3D bioprinting. *Biofabrication*. 2016;8(3):032002.

    doi: 10.1088/1758-5090/8/3/032002

14. Lee JM, Ng WL, Yeong WY. Resolution and shape in bioprinting: Strategizing towards complex tissue and organ printing. *Appl Phys Rev*. 2019;6(1):011306.

    doi: 10.1063/1.5053909

15. Fu Z, Naghieh S, Xu C, Wang C, Sun W, Chen X. Printability in extrusion bioprinting. *Biofabrication*. 2021;13(3):033001.

    doi: 10.1088/1758-5090/abe7ab

16. Wu D, Zheng K, Yin W, *et al*. Enhanced osteochondral regeneration with a 3D-Printed biomimetic scaffold featuring a calcified interfacial layer. *Bioact Mater*. 2024;36:317-329.

    doi: 10.1016/j.bioactmat.2024.03.004

17. Liu Y, Peng L, Li L, *et al*. 3D-bioprinted BMSC-laden biomimetic multiphasic scaffolds for efficient repair of osteochondral defects in an osteoarthritic rat model. *Biomaterials*. 2021;279:121216.

    doi: 10.1016/j.biomaterials.2021.121216

18. Lesage C, Lafont M, Guihard P, Weiss P, Guicheux J, Delplace V. Material-Assisted Strategies for Osteochondral Defect Repair. *Adv Sci*. 2022;9(16):2200050.

    doi: 10.1002/advs.202200050

19. Baumann CA, Hinckel BB, Bozynski CC, Farr J. Articular Cartilage: Structure and Restoration. In: *Joint Preservation of the Knee: A Clinical Casebook*. Cham, Switzerland: Springer International Publishing; 2019:3-24.

    doi: 10.1007/978-3-030-01491-9_1

20. Norrdin R, Kawcak C, Capwell B, McIlwraith C. Calcified cartilage morphometry and its relation to subchondral bone remodeling in equine arthrosis. *Bone*. 1999;24(2):109-114.

    doi: 10.1016/S8756-3282(98)00157-4

21. Zhou L, Gjvm VO, Malda J, *et al*. Innovative Tissue-Engineered Strategies for Osteochondral Defect Repair and Regeneration: Current Progress and Challenges. *Adv Healthc Mater*. 2020;9(23):2001008.

    doi: 10.1002/adhm.202001008

22. Goyal D, Goyal A, Adachi N. Subchondral bone: healthy soil for the healthy cartilage. In: *Bio-orthopaedics*. Berlin, Germany: Springer; 2017:479-486.

    doi: 10.1007/978-3-662-54181-4_38

23. Zhang B, Huang J, Narayan RJ. Gradient scaffolds for osteochondral tissue engineering and regeneration. *J Mater Chem B*. 2020;8(36):8149-8170.

    doi: 10.1039/D0TB00688B

24. Cole BJ, Malek MM. *Articular Cartilage Lesions: A Practical Guide to Assessment and Treatment*. New York, NY: Springer Science & Business Media; 2004.

25. Cheuk YC, Wong MWN, Lee KM, Fu SC. Use of allogeneic scaffold-free chondrocyte pellet in repair of osteochondral defect in a rabbit model. *J Orthop Res*. 2011;29(9):1343-1350.

    doi: 10.1002/jor.21339

26. Li H, Qian J, Chen J, Zhong K, Chen S. Osteochondral repair with synovial membranederived mesenchymal stem cells. *Mol Med Rep*. 2016;13(3):2071-2077.

    doi: 10.3892/mmr.2016.4795

27. Wang X, Song X, Li T, *et al*. Aptamer-functionalized bioscaffold enhances cartilage repair by improving stem cell recruitment in osteochondral defects of rabbit knees. *Am J Sports Med*. 2019;47(10):2316-2326.

    doi: 10.1177/0363546519856355

28. Jeong CG, Zhang H, Hollister SJ. Three-dimensional polycaprolactone scaffold-conjugated bone morphogenetic protein-2 promotes cartilage regeneration from primary chondrocytes in vitro and in vivo without accelerated endochondral ossification. *J Biomed Mater Res A*. 2012;100(8):2088-2096.

    doi: 10.1002/jbm.a.33249

29. Pati F, Jang J, Lee JW, Cho D-W. Extrusion bioprinting. In: Atala A, Yoo JJ, eds. *Essentials of 3D Biofabrication and Translation*. Amsterdam, Netherlands: Elsevier; 2015:123-152.

    doi: 10.1016/B978-0-12-800972-7.00007-4

30. Mandrycky C, Wang Z, Kim K, Kim D-H. 3D bioprinting for engineering complex tissues. *Biotechnol Adv*. 2016;34(4):422-434.

    doi: 10.1016/j.biotechadv.2015.12.011

31. Boularaoui S, Al Hussein G, Khan KA, Christoforou N, Stefanini C. An overview of extrusion-based bioprinting with a focus on induced shear stress and its effect on cell viability. *Bioprinting*. 2020;20:e00093.

    doi: 10.1016/j.bprint.2020.e00093

32. Costantini M, Colosi C, Święszkowski W, Barbetta A. Co-axial wet-spinning in 3D bioprinting: state of the art and future perspective of microfluidic integration. *Biofabrication*. 2018;11(1):012001.

    doi: 10.1088/1758-5090/aae605

33. Wu Z, Yao H, Sun H, *et al*. Enhanced hyaline cartilage formation and continuous osteochondral regeneration via 3D-Printed heterogeneous hydrogel with multi-crosslinking inks. *Mater Today Bio*. 2024;26:101080.

    doi: 10.1016/j.mtbio.2024.101080

34. Khalil S, Sun W. Bioprinting endothelial cells with alginate for 3D tissue constructs. *J Biomech Eng*. 2009;131(11):111002.

    doi: 10.1115/1.3128729

35. Cornock R, Beirne S, Thompson B, Wallace G. Coaxial additive manufacture of biomaterial composite scaffolds for tissue engineering. *Biofabrication*. 2014;6(2):025002.

    doi: 10.1088/1758-5082/6/2/025002

36. Jin Y, Compaan A, Bhattacharjee T, Huang Y. Granular gel support-enabled extrusion of three-dimensional alginate and cellular structures. *Biofabrication*. 2016;8(2):025016.

    doi: 10.1088/1758-5090/8/2/025016

37. Gao G, Kim BS, Jang J, Cho D-W. Recent strategies in extrusion-based three-dimensional cell printing toward organ biofabrication. *ACS Biomater Sci Eng*. 2019;5(3):1150-1169.

    doi: 10.1021/acsbiomaterials.8b00691

38. Moroni L, Boland T, Burdick JA, *et al*. Biofabrication: a guide to technology and terminology. *Trends Biotechnol*. 2018;36(4):384-402.

    doi: 10.1016/j.tibtech.2017.10.015

39. Habib A, Sathish V, Mallik S, Khoda B. 3D Printability of Alginate-Carboxymethyl Cellulose Hydrogel. *Materials*. 2018;11(3):454.

    doi: 10.3390/ma11030454

40. Ramirez Caballero SS, Saiz E, Montembault A, *et al*. 3-D printing of chitosan-calcium phosphate inks: rheology, interactions and characterization. *J Mater Sci Mater Med*. 2019;30(1):1-15.

    doi: 10.1007/s10856-018-6201-y

41. Mezger T. *The Rheology Handbook: For Users of Rotational and Oscillatory Rheometers*. 5th ed. Hannover, Germany: European Coatings; 2020.

42. Mouser VH, Melchels FP, Visser J, Dhert WJ, Gawlitta D, Malda J. Yield stress determines bioprintability of hydrogels based on gelatin-methacryloyl and gellan gum for cartilage bioprinting. *Biofabrication*. 2016;8(3):035003.

    doi: 10.1088/1758-5090/8/3/035003

43. Highley CB, Song KH, Daly AC, Burdick JA. Jammed microgel inks for 3D printing applications. *Adv Sci*. 2019;6(1):1801076.

    doi: 10.1002/advs.201801076

44. Schwartz R, Malpica M, Thompson GL, Miri AK. Cell encapsulation in gelatin bioink impairs 3D bioprinting resolution. *J Mech Behav Biomed Mater*. 2020;103:103524.

    doi: 10.1016/j.jmbbm.2019.103524

45. Lee A, Hudson A, Shiwarski D, *et al*. 3D bioprinting of collagen to rebuild components of the human heart. *Science*. 2019;365(6452):482-487.

    doi: 10.1126/science.aav9051

46. Gillispie G, Prim P, Copus J, *et al*. Assessment methodologies for extrusion-based bioink printability. *Biofabrication*. 2020;12(2):022003.

    doi: 10.1088/1758-5090/ab6f0d

47. Ribeiro A, Blokzijl MM, Levato R, *et al*. Assessing bioink shape fidelity to aid material development in 3D bioprinting. *Biofabrication*. 2017;10(1):014102.

doi: 10.1088/1758-5090/aa90e2

48. Bercea M. Rheology as a tool for fine-tuning the properties of printable bioinspired gels. *Molecules*. 2023;28(6):2766.

doi: 10.3390/molecules28062766

49. Paxton N, Smolan W, Böck T, Melchels F, Groll J, Jungst T. Proposal to assess printability of bioinks for extrusion-based bioprinting and evaluation of rheological properties governing bioprintability. *Biofabrication*. 2017;9(4):044107.

doi: 10.1088/1758-5090/aa8dd8

50. Peak CW, Stein J, Gold KA, Gaharwar AK. Nanoengineered colloidal inks for 3D bioprinting. *Langmuir*. 2018;34(3):917-925.

doi: 10.1021/acs.langmuir.7b02540

51. Sarker M, Naghieh S, McInnes AD, Ning L, Schreyer DJ, Chen X. Bio-fabrication of peptide-modified alginate scaffolds: Printability, mechanical stability and neurite outgrowth assessments. *Bioprinting*. 2019;14:e00045.

doi: 10.1016/j.bprint.2019.e00045

52. Müller M, Fisch P, Molnar M, *et al*. Development and thorough characterization of the processing steps of an ink for 3D printing for bone tissue engineering. *Mater Sci Eng C*. 2020;108:110510.

doi: 10.1016/j.msec.2019.110510

53. Ouyang L, Yao R, Zhao Y, Sun W. Effect of bioink properties on printability and cell viability for 3D bioplotting of embryonic stem cells. *Biofabrication*. 2016;8(3):035020.

doi: 10.1088/1758-5090/8/3/035020

54. Therriault D, White SR, Lewis JA. Rheological behavior of fugitive organic inks for direct-write assembly. *Appl Rheol*. 2007;17(1):10112-1-10112-8.

doi: 10.1515/arh-2007-0001

55. Wang L, Xu M, Zhang L, Zhou Q, Luo L. Automated quantitative assessment of three-dimensional bioprinted hydrogel scaffolds using optical coherence tomography. *Biomed Opt Express*. 2016;7(3):894-910.

doi: 10.1364/BOE.7.000894

56. Chen C-W, Betz MW, Fisher JP, Paek A, Chen Y. Macroporous hydrogel scaffolds and their characterization by optical coherence tomography. *Tissue Eng Part C Methods*. 2011;17(1):101-112.

doi: 10.1089/ten.TEC.2010.0072

57. Menon A, Póczos B, Feinberg AW, Washburn NR. Optimization of silicone 3D printing with hierarchical machine learning. *3D Print Addit Manuf*. 2019;6(4):181-189.

doi: 10.1089/3dp.2018.0088

58. Tomasina C, Bodet T, Mota C, Moroni L, Camarero-Espinosa S. Bioprinting vasculature: materials, cells and emergent techniques. *Materials*. 2019;12(17):2701.

doi: 10.3390/ma12172701

59. Ouyang L. Pushing the rheological and mechanical boundaries of extrusion-based 3D bioprinting. *Trends Biotechnol*. 2022;40(7):891-902.

doi: 10.1016/j.tibtech.2022.01.001

60. Seiffert S, Sprakel J. Physical chemistry of supramolecular polymer networks. *Chem Soc Rev*. 2012;41(2):909-930.

doi: 10.1039/C1CS15191F

61. Cui X, Li J, Hartanto Y, *et al*. Advances in extrusion 3D bioprinting: a focus on multicomponent hydrogel-based bioinks. *Adv Healthc Mater*. 2020;9(15):1901648.

doi: 10.1002/adhm.201901648

62. Drury JL, Mooney DJ. Hydrogels for tissue engineering: scaffold design variables and applications. *Biomaterials*. 2003;24(24):4337-4351.

doi: 10.1016/S0142-9612(03)00340-5

63. Lan X, Ma Z, Dimitrov A, *et al*. Double crosslinked hyaluronic acid and collagen as a potential bioink for cartilage tissue engineering. *Int J Biol Macromol*. 2024;273:132819.

doi: 10.1016/j.ijbiomac.2024.132819

64. Hashemi-Afzal F, Bagheri F, Vasheghani-Farahani E, Azami M, Tayebi L, Eslaminejad MB. 3D-bioprinted dual-crosslinked oxidized gellan gum-decellularized human amniotic membrane hydrogels reinforced with aminolyzed electrospun nanofibers for cartilage regeneration. *Biomater Adv*. 2026;182:214654.

doi: 10.1016/j.bioadv.2025.214654

65. Çelik E, Bayram C, Denkbaş EB. Zone-inspired hydrogel constructs promote spatially controlled chondrogenesis for osteochondral regeneration. *Sci Rep*. 2025;16(1):3370.

doi: 10.1038/s41598-025-33222-0

66. Lombardi L, Scalzone A, Ausilio C, Gentile P, Tammaro D. Optimizing nozzle design in extrusion-based 3D bioprinting to minimize mechanical stress and enhance cell viability. *Int J Bioprint*. 2025;0(0):025190182.

doi: 10.36922/IJB025190182

67. Wei Q, An Y, Zhao X, Li M, Zhang J, Cui N. Optimal design of multi-biomaterials mixed extrusion nozzle for 3D bioprinting considering cell activity. *Virtual Phys Prototyping*. 2025;20(1):e2438897.

doi: 10.1080/17452759.2024.2438897

68. Afghah F, Kheiri S, Ladd A, *et al*. Advancing bioink homogeneity in extrusion 3D bioprinting with active in situ magnetic mixing. *Device*. 2026;4(3):101044.

doi: 10.1016/j.device.2025.101044

69. Li X, Chen S, Li J, *et al*. 3D culture of chondrocytes in gelatin

hydrogels with different stiffness. *Polymers*. 2016;8(8):269.

doi: 10.3390/polym8080269

70. Nicodemus G, Skaalure S, Bryant S. Gel structure has an impact on pericellular and extracellular matrix deposition, which subsequently alters metabolic activities in chondrocyte-laden PEG hydrogels. *Acta Biomater*. 2011;7(2):492-504.

doi: 10.1016/j.actbio.2010.08.021

71. Hosseini M, Dimaraki A, van Osch GJ, Fratila-Apachitei LE, Díaz-Payno PJ, Zadpoor AA. Three-Dimensional Bioprinting of Regenerative Cartilage Constructs with Directional Ionically Derived Stiffness Gradients. *J Funct Biomater*. 2025;16(12):451.

doi: 10.3390/jfb16120451

72. Ai C, Liu L, Wong K, Tan XH, Goh JC. The effect of chondroitin sulfate concentration and matrix stiffness on chondrogenic differentiation of mesenchymal stem cells. *Biomater Sci*. 2023;11(13):4557-4573.

doi: 10.1039/D2BM01980A

73. Tavakoli S, Krishnan N, Mokhtari H, Oommen OP, Varghese OP. Fine-tuning dynamic cross–linking for enhanced 3D bioprinting of hyaluronic acid hydrogels. *Adv Funct Mater*. 2024;34(4):2307040.

doi: 10.1002/adfm.202307040

74. Tavakoli S, Kocatürkmen A, Oommen OP, Varghese OP. Ultra-fine 3D bioprinting of dynamic hyaluronic acid hydrogel for in vitro modeling. *Adv Mater*. 2025;37(30):2500315.

doi: 10.1002/adma.202500315

75. Distler T, Solisito AA, Schneidereit D, Friedrich O, Detsch R, Boccaccini AR. 3D printed oxidized alginate-gelatin bioink provides guidance for C2C12 muscle precursor cell orientation and differentiation via shear stress during bioprinting. *Biofabrication*. 2020;12(4):045005.

doi: 10.1088/1758-5090/ab98e4

76. Wang B, Diaz-Payno PJ, Browe DC, *et al*. Affinity-bound growth factor within sulfated interpenetrating network bioinks for bioprinting cartilaginous tissues. *Acta Biomater*. 2021;128:130-142.

doi: 10.1016/j.actbio.2021.04.016

77. Schipani R, Scheurer S, Florentin R, Critchley SE, Kelly DJ. Reinforcing interpenetrating network hydrogels with 3D printed polymer networks to engineer cartilage mimetic composites. *Biofabrication*. 2020;12(3):035011.

doi: 10.1088/1758-5090/ab8708

78. Wang D, Zeng J, Zhu H, *et al*. Extrusion bioprinting of elastin-containing bioactive double-network tough hydrogels for complex elastic tissue regeneration. *Aggregate*. 2024;5(3):e477.

doi: 10.1002/agt2.477

79. Zhang Y, Li D, Liu Y, *et al*. 3D-bioprinted anisotropic bicellular living hydrogels boost osteochondral regeneration via reconstruction of cartilage–bone interface. *Innovation*. 2024;5(1):100542.

doi: 10.1016/j.xinn.2023.100542

80. Sasikumar SC, Goswami U, Raichur AM. Mucin-based dual cross-linkable IPN hydrogel bioink for 3D bioprinting and cartilage tissue engineering. *ACS Appl Bio Mater*. 2025;8(2):1186-1200.

doi: 10.1021/acsabm.4c01505

81. Chandra DK, Reis RL, Kundu SC, Kumar A, Mahapatra C. Nanomaterials-based hybrid bioink platforms in advancing 3D bioprinting technologies for regenerative medicine. *ACS Biomater Sci Eng*. 2024;10(7):4145-4174.

doi: 10.1021/acsbiomaterials.4c00166

82. Amhare AF, Qiao L, Deng H, *et al*. The current status of nano-hydrogel preparations for osteochondral repair: Systematic Review. *Front Bioeng Biotechnol*. 2025;13:1611522.

doi: 10.3389/fbioe.2025.1611522

83. Lu J, Gao Y, Cao C, *et al*. 3D bioprinted scaffolds for osteochondral regeneration: advancements and applications. *Mater Today Bio*. 2025;32:101834.

doi: 10.1016/j.mtbio.2025.101834

84. Corzo IJM, da Fonseca JHL, Ferman V, Sánchez DNR, de Oliveira ALR, d'Ávila MA. Optimizing biomaterial inks: A study on the printability of Carboxymethyl cellulose-Laponite nanocomposite hydrogels and dental pulp stem cells bioprinting. *Bioprinting*. 2024;43:e00358.

doi: 10.1016/j.bprint.2024.e00358

85. Chimene D, Kaunas R, Gaharwar AK. Hydrogel bioink reinforcement for additive manufacturing: a focused review of emerging strategies. *Adv Mater*. 2020;32(1):1902026.

doi: 10.1002/adma.201902026

86. Kosowska K, Korycka P, Jankowska-Snopkiewicz K, *et al*. Graphene oxide (GO)-based bioink with enhanced 3D printability and mechanical properties for tissue engineering applications. *Nanomaterials*. 2024;14(9):760.

doi: 10.3390/nano14090760

87. Chakraborty J, Fernandez-Perez J, Ghahfarokhi MT, *et al*. Development of 4D-bioprinted shape-morphing magnetic constructs for cartilage regeneration using a silk fibroin-gelatin bioink. *Cell Rep Phys Sci*. 2024;5(3):101819.

doi: 10.1016/j.xcrp.2024.101819

88. Zengin A, Teixeira FC, Feliciano T, *et al*. Matrix metalloproteinase degradable, in situ photocrosslinked nanocomposite bioinks for bioprinting applications. *Biomater Adv*. 2023;154:213647.

doi: 10.1016/j.bioadv.2023.213647

89. Zengin A, Hafeez S, Habibovic P, Baker M, van Rijt S. Extracellular matrix mimetic supramolecular hydrogels reinforced with covalent crosslinked mesoporous silica nanoparticles. *J Mater Chem B*. 2024;12(48):12577-12588.

doi: 10.1039/D4TB00499J

90. Landau S, Kieda J, Khosravi R, *et al*. Cell driven elastomeric particle packing in composite bioinks for engineering and implantation of stable 3D printed structures. *Bioact Mater*. 2025;44:411-427.

doi: 10.1016/j.bioactmat.2024.10.008

91. Xu R, Ooi HS, Bian L, Ouyang L, Sun W. Dynamic hydrogels for biofabrication: A review. *Biomaterials*. 2025;320:123266.

doi: 10.1016/j.biomaterials.2025.123266

92. Dai W, Gong X, Wang C, *et al*. Injectable decellularized extracellular matrix hydrogel with cell-adaptable supramolecular network enhances cartilage regeneration by regulating inflammation and facilitating chondrogenesis. *Chem Eng J*. 2024;498:155138.

doi: 10.1016/j.cej.2024.155138

93. Xu J, Feng Q, Lin S, *et al*. Injectable stem cell-laden supramolecular hydrogels enhance in situ osteochondral regeneration via the sustained co-delivery of hydrophilic and hydrophobic chondrogenic molecules. *Biomaterials*. 2019;210:51-61.

doi: 10.1016/j.biomaterials.2019.04.031

94. Ma X, Yang R, Wang P, *et al*. Bioinspired dual dynamic network hydrogels promote cartilage regeneration through regulating BMSC chondrogenic differentiation. *Mater Today Chem*. 2022;23:100648.

doi: 10.1016/j.mtchem.2021.100648

95. Ravi S, Chokkakula LP, Dey SR, Rath SN. Fabrication of hypoxia-mimicking supramolecular hydrogels for cartilage repair. *ACS Appl Bio Mater*. 2025;8(2):1261-1277.

doi: 10.1021/acsabm.4c01576

96. Falandt M, Nunez Bernal P, Longoni A, *et al*. Hybrid supramolecular-covalent bioresin promotes cell migration and self-assembly in light-based volumetric bioprinted constructs. *bioRxiv*. Preprint posted online 2025.

doi: 10.1101/2025.01.06.631505

97. Stampoultzis T, Rana VK, Guo Y, Pioletti DP. Impact of molecular dynamics of polyrotaxanes on chondrocytes in double-network supramolecular hydrogels under physiological thermomechanical stimulation. *Biomacromolecules*. 2024;25(2):1144-1152.

doi: 10.1021/acs.biomac.3c01132

98. Lewis JA, Nemke B, Lu Y, *et al*. A bioactive supramolecular and covalent polymer scaffold for cartilage repair in a sheep model. *Proc Natl Acad Sci USA*. 2024;121(33):e2405454121.

doi: 10.1073/pnas.2405454121

99. Grivet-Brancot A, Boffito M, Ciardelli G. Use of polyesters in fused deposition modeling for biomedical applications. *Macromol Biosci*. 2022;22(10):2200039.

doi: 10.1002/mabi.202200039

100. Wang F-Z, Liu S, Gao M, *et al*. 3D-printed polycaprolactone/hydroxyapatite bionic scaffold for bone regeneration. *Polymers*. 2025;17(7):858.

doi: 10.3390/polym17070858

101. Ke Re Mu ALM, Liang ZL, Chen L, Tu Xun AKBE, A Bu Li Ke Mu MMTAL, Wu YQ. 3D printed PLGA scaffold with nano-hydroxyapatite carrying linezolid for treatment of infected bone defects. *Biomed Pharmacother*. 2024;172:116228.

doi: 10.1016/j.biopha.2024.116228

102. Du M, Tronci G, Yang XB, Wood DJ. Parameter Optimisation in 3D Extrusion Printing of Polyhydroxybutyrate Using Design of Experiment Methodology. *J Funct Biomater*. 2026;17(2):90.

doi: 10.3390/jfb17020090

103. Kim D, Lee SJ, Lee D, *et al*. Biomimetic mineralization of 3D-printed polyhydroxyalkanoate-based microbial scaffolds for bone tissue engineering. *Int J Bioprint*. 2024;10(1):1806.

doi: 10.36922/ijb.1806

104. Cheng R, Xie T, Ma W, *et al*. Application of polydopamine-modified triphasic PLA/PCL-PLGA/Mg (OH) 2-velvet antler polypeptides scaffold loaded with fibrocartilage stem cells for the repair of osteochondral defects. *Front Bioeng Biotechnol*. 2024;12:1460623.

doi: 10.3389/fbioe.2024.1460623

105. Cantella S, Badini S, Bollati C, *et al*. Development of a 3D-printable bioactive polycaprolactone–collagen peptides filament for biomedical applications. *Sci Rep*. 2025;15(1):44513.

doi: 10.1038/s41598-025-28030-5

106. Xu Z, Zhang Y, Dai H, *et al*. 3D printed MXene (Ti2AlN)/polycaprolactone composite scaffolds for in situ maxillofacial bone defect repair. *J Ind Eng Chem*. 2022;114:536-548.

doi: 10.1016/j.jiec.2022.07.042

107. Wang Y, Ling C, Chen J, *et al*. 3D-printed composite scaffold with gradient structure and programmed biomolecule delivery to guide stem cell behavior for osteochondral regeneration. *Biomater Adv*. 2022;140:213067.

doi: 10.1016/j.bioadv.2022.213067

108. Mackay ME. The importance of rheological behavior in the additive manufacturing technique material extrusion. *J Rheol*. 2018;62(6):1549-1561.

doi: 10.1122/1.5037687

109. Balani SB, Ghaffar SH, Chougan M, Pei E, Şahin E. Processes and materials used for direct writing technologies: A review. *Results Eng*. 2021;11:100257.

doi: 10.1016/j.rineng.2021.100257

110. Gu P, Xu Y, Liu Q, *et al*. Tailorable 3DP flexible scaffolds with porosification of filaments facilitate cell ingrowth and biomineralized deposition. *ACS Appl Mater Interfaces*. 2022;14(29):32914-32926.

doi: 10.1021/acsami.2c07649

111. Zhang B, Chung SH, Barker S, Craig D, Narayan RJ, Huang J. Direct ink writing of polycaprolactone/polyethylene oxide based 3D constructs. *Prog Nat Sci Mater Int*. 2021;31(2):180-191.

doi: 10.1016/j.pnsc.2020.10.001

112. Tolbert JW, French T, Kitson A, *et al*. Solvent-cast 3D printing with molecular weight polymer blends to decouple effects of scaffold architecture and mechanical properties on mesenchymal stromal cell fate. *J Biomed Mater Res A*. 2024;112(9):1364-1375.

doi: 10.1002/jbm.a.37674

113. Russias J, Saiz E, Deville S, *et al*. Fabrication and in vitro characterization of three-dimensional organic/inorganic scaffolds by robocasting. *J Biomed Mater Res A*. 2007;83(2):434-445.

doi: 10.1002/jbm.a.31237

114. International Council for Harmonisation. ICH Q3C(R9): Impurities: Guideline for Residual Solvents. 2024. Accessed May 14, 2026. https://database.ich.org/sites/default/files/ICH_Q3C%28R9%29_Guideline_MinorRevision_2024_2024_Approved.pdf

115. Villanueva Navarrete D, Sandoval-Castellanos AM, Gunen M, *et al*. Wetstable PLGA–PCL electrospun membranes as synthetic scaffolds for corneal applications. *Biomed Mater*. 2026;21(2):025033.

doi: 10.1088/1748-605X/ae57f1

116. Nam J, Huang Y, Agarwal S, Lannutti J. Materials selection and residual solvent retention in biodegradable electrospun fibers. *J Appl Polym Sci*. 2008;107(3):1547-1554.

doi: 10.1002/app.27063

117. Liu H, Dou Y, Wei J, *et al*. Fiber-reinforced hydrogel combined with 3D printed scaffolds for regeneration of osteochondral defects. *Mater Chem Phys*. 2025;335:130532.

doi: 10.1016/j.matchemphys.2025.130532

118. Wang H, Zhang J, Bai H, *et al*. 3D printed cell-free bilayer porous scaffold based on alginate with biomimetic microenvironment for osteochondral defect repair. *Biomater Adv*. 2025;167:214092.

doi: 10.1016/j.bioadv.2024.214092

119. Gu E, Chen K, Zheng J, *et al*. 3D-printed GelMA/BC@PLLAms-Cur@ TCP-PCL-PEG bilayer scaffold for osteochondral repair. *RSC Adv*. 2026;16(15):13949-13959.

doi: 10.1039/D5RA07655B

120. Ghorbani F, Oliveira JM, Qian Z, *et al*. Biomimetically hierarchical scaffolds drive critical-sized osteochondral tissue regeneration. *Int J Bioprint*. 2025;11(1):573-597.

doi: 10.36922/ijb.5104

121. Mahajan A, Zaidi ZS, Shukla A, Saxena R, Katti DS. Functionally graded hydrogels with opposing biochemical cues for osteochondral tissue engineering. *Biofabrication*. 2024;16(3):035020.

doi: 10.1088/1758-5090/ad467e

122. Zhao X, Wang W, Yu X, Kalyon DM, Erisken C. Bioextrusion of hydrogels with controlled mineral gradients for regenerative engineering of osteochondral interfaces. *Bio-Des Manuf*. 2026;9(1):122-136.

doi: 10.1631/bdm.2500291

123. Huang Y, Fan H, Gong X, Yang L, Wang F. Scaffold With Natural Calcified Cartilage Zone for Osteochondral Defect Repair in Minipigs. *Am J Sports Med*. 2021;49(7):1883-1891.

doi: 10.1177/03635465211007139

124. Wang Y, Hou Y, Vyas C, Huang B, Bartolo P. An integrated hybrid 3D bioprinting of heterogeneous and zone-specific construct resembling structural and biofunctional properties of osteochondral tissue. *Mater Futures*. 2025;4(2):025401.

doi: 10.1088/2752-5724/adb7f6

125. U.S. Food and Drug Administration. Technical Considerations for Additive Manufactured Medical Devices: Guidance for Industry and Food and Drug Administration Staff. 2017. Accessed May 14, 2026. https://www.fda.gov/regulatory-information/search-fda-guidance-documents/technical-considerations-additive-manufactured-medical-devices